ETH
Eidgenössische Technische Hochschule Zürich
Swiss Federal Institute of Technology Zurich

Master Thesis

TRAJECTORY SIMULATIONS OF RYDBERG ATOMS FOR A HYBRID CAVITY QED EXPERIMENT

Christian Gross

September 2010

Supervisor
Dr. Stefan Filipp

Principal Investigator
Prof. Dr. Andreas Wallraff

Abstract

Quantum systems in their most elementary form follow the rather bizarre concepts of superposition and entanglement. In the early days of quantum mechanics, these effects were believed to be a purely theoretical oddment, that could never be observed. The argument was that one never experiments with just one atom or electron, but always only with an ensemble of them. The advances both in theoretical description and experimental techniques though, allowed to observe these phenomena in various systems and pushed forward the realization of a quantum computer. There, the classical bit is replaced by the qubit, its quantum counterpart, which can in principle be any two-level quantum system. In practice these qubits need to meet different criteria [1], which in real systems are difficult to fulfill simultaneously. All physical systems have individual advantages, but they are usually intrinsically related to their biggest drawbacks. A proposed new strategy to overcome this problem is to combine two different qubit implementations to profit, e.g., both from fast qubit manipulations in solid state devices and long coherence times of atomic degrees of freedom.

This thesis is part of a project that aims to implement an interface between superconducting qubits and highly excited Rydberg atoms. In this architecture, the internal state of the atoms serves as long-lived memory of the quantum state of a superconducting qubit. The two systems are coupled by the strong electric fields in a transmission line resonator.
In this work the trajectories of an ensemble of Rydberg atoms traversing the experimental setup and their subsequent detection is simulated. These simulations are of importance both for the optimization of the setup, as well as for the evaluation of the experimental results. In particular, a geometry for guiding of a beam of Rydberg atoms has been devised. With the simulation program it was shown, that the proposed on-chip quadrupole guide allows to focus the beam onto the detector. The experimental demonstration will be the basis for future on-chip beam manipulation techniques.

Contents

1. Introduction

Quantum mechanics was developed in the last century and has since then proven to be a highly successful theory. Many of today's everyday applications are based on the deep understanding of the microscopic world, made accessible by the advent of quantum theory. The probably most influential example of such an application is the computer. Its processor is based on billions of semiconductor elements, which allow to perform simple logical operations.
In such an operation many electrons generate an electrical current. Even if quantum concepts are necessary to describe these processes, the most intriguing and at the same time most counter-intuitive aspects of quantum mechanics are hidden, such as the entanglement and the superposition principle for example. They implicitly imply the non-locality of quantum mechanics, which has lead to controversial discussions about the completeness of this theory [2]. However, many experiments have since then been conducted to resolve this issue. All of them confirmed the 'strange' predictions of quantum theory [3, 4, 5].
In 1982 Richard Feynman proposed a new kind of computer based on these properties. This 'quantum computer' would allow to simulate a large quantum mechanical system, a task that cannot be performed efficiently on a classical computer [6]. Subsequently, Shor presented a quantum algorithm [7] to factorize large numbers, which is exponentially faster than its classical counterpart. Apart from showing that a quantum computer can be more powerful for particular tasks, this algorithm is of practical interest, as it could be used to break public-key cryptography [8].
Quantum computation and information is – as defined in Ref. [8] – the study of information processing tasks that can be accomplished using quantum mechanical systems. Even though this appears to be quite straightforward, the experimental realization of such a system turned out to be rather challenging. The conditions that need to be met by such a system are given by the DiVincenzo criteria [1] and there are several candidates which could serve as quantum bits (qubits). The most prominent systems that have the potential to fulfill these requirements are probably trapped ions [9], quantum dots [10] and superconducting qubits [11].

Cavity quantum electrodynamics

Quantum electrodynamics (QED) is the theory describing the interaction of light and matter [12]. An atom in free space is subject to spontaneous decay due to its coupling to radiation modes in vacuum. In free space, these modes form a continuum in the frequency space, but by imposing boundary conditions it is possible to modify their spatial and frequency distribution

with discrete mode structure.
This leads to what is known as cavity QED, which studies the interaction of the quantized electromagnetic radiation inside a cavity with atoms. In the most pure form a single atom interacts coherently with a single photon in the strong coupling regime. In this case the excited atom will emit one photon into the initially empty cavity, which will be trapped for some time and then be reabsorbed by the same atom. The atom and the cavity share one 'quantum' of energy and this process is known as vacuum Rabi oscillation [13]. Such a system has successfully been realized with a single ^{27}Rb atom coupled to a high-finesse optical cavity [14].
A strongly coupled cavity QED system can as well be achieved in a solid state environment as proposed in Ref. [15]. Experimentally this was realized by coupling a superconducting two-level system to a one dimensional transmission line resonator [16].
Superconducting qubits have become an increasingly acknowledged candidate for quantum information processing. The basis for this success is the very strong coupling of the two-level system or artificial atom to the electromagnetic radiation in the cavity, which allows for fast operations. A main challenge, however, remains the coherence time. As the system is embedded in a solid state environment, it is subject to interaction with the environment leading to fast decoherence, which seems difficult to overcome [17]. Nevertheless, the implementation of simple quantum algorithms has recently been demonstrated in a two-qubit superconducting processor [18].

Hybrid Systems

The main goal of combining different experimental approaches for quantum information tasks is to make use of the individual advantages in each system. Due to the excellent isolation from the environment, the coherence time of atomic degrees of freedom can be very long [9]. On the other hand, the small size of single atoms leads to a weak interaction with electromagnetic radiation, making it difficult to access them in the experiment. The situation is reversed for superconducting qubits, where the main characteristics are the strong coupling and the relatively short coherence time. It is therefore interesting to consider ways to merge the virtues of these two systems.
Different approaches were proposed recently, such as to couple an ensemble of trapped polar molecules to a transmission line resonator [19]. The molecules would serve as a quantum memory with a long lifetime, while strongly coupled to the cavity modes. Another proposal suggests to capacitively couple a transmission line resonator to a temporarily excited Rydberg atom, making use of their large dipole moment [20].

This thesis is part of a long term project with the objective to develop such a hybrid system for quantum information processing. In particular one aims to investigate the coherent

coupling of atomic with solid state degrees of freedom, where the internal atomic states of interest are different Stark states of highly excited Rydberg atoms.
These states exhibit a huge electric dipole moment which is a crucial requirement to achieve strong coupling to microwave photons in a circuit QED environment. The transition frequency between two adjacent Rydberg states is determined by their principal quantum number n and is below ≈ 50 GHz for $n \geq 50$. This is within the reach of current circuit QED setups. Combined with the long coherence time of these Rydberg states, they seem to be an optimal choice to realize an atom - solid state interface for future quantum information applications.
In first experiments a beam of hydrogen atoms excited to Rydberg states will be prepared and investigated [21]. The effects of the interaction with surfaces of different materials will be studied along with their distance dependence. Subsequently, the atom beam will be exposed to the microwave field of a transmission line resonator. This radiation will induce excitations from the n to the $n+1$ Rydberg level, if the applied frequency is resonant with this transition. Such changes in the principal quantum number of the Rydberg atom can be detected with the experimentally well established state selective field ionization [22].
These early results shall then pave the way towards more elaborate experimental schemes, aiming to decelerate and to trap a single Rydberg atom in the vicinity of a transmission line resonator and to coherently couple these two systems. Ultimately this will allow to transfer quantum information from a superconducting qubit to an atomic qubit, serving as quantum memory with a long coherence time. At the same time, the advantage of fast operation times of superconducting qubits will be preserved.

2. Rydberg Atoms

2.1. Historical Background

In 1860, roughly speaking half a century before the birth of quantum mechanics, the chemist Robert Bunsen and the physicist Gustav Kirchhoff discovered that each chemical element has its very own emission spectrum. In their experiments they found that a hot tenuous gas emits light only at a number of well defined wavelengths, comparable to an optical fingerprint for each element.
Though not understanding the underlying physics of this phenomenon, Johann Balmer found 15 years later a relation predicting accurately the emission wavelength λ of the hydrogen atom [23],

$$\lambda = \frac{bn^2}{n^2 - 4} \tag{2.1}$$

where $b = 364.56\,\text{nm}$ and n a natural number larger than two. By rewriting this equation in terms of the inverse wavelength $\frac{1}{\lambda}$ and by replacing 4 by 2^2 one can realize that it returns the wavelengths of transitions from higher lying levels to the $n = 2$ level. The ensemble of all those lines is called the Balmer series and lies partially in the visible range.
By further substituting $\frac{4}{b}$ with R_H and by generalizing the final state from $n' = 2$ to an arbitrary $n' < n$ we arrive at the Rydberg formula [24]

$$\frac{1}{\lambda} = R_H \left(\frac{1}{n'^2} - \frac{1}{n^2} \right), \tag{2.2}$$

where $R_H = 1.09678 \times 10^7\ \text{m}^{-1}$ [24]. By the time when Johannes Rydberg published this formula in 1889, it could indeed predict all the spectral lines of the hydrogen atom with very high accuracy, but the natural numbers n and n' did not yet have a physical interpretation. The link between the puzzling occurrence of the spectral lines and their excellent prediction, was missing for many years to come, until Niels Bohr proposed his model for the hydrogen atom in 1913.
In this model the electron moves in circular orbits around the proton. In addition to the classical laws of physics, he imposed two further assumption. The first one was that the electron did not continuously emit radiation, which was a requirement for stable orbits. The second one was to quantize the angular momentum, which was motivated by the fact that the spectral lines occurred at discrete wavelengths. By considering the total energy of each orbit, he found a relation for the allowed transition energies given by [23]

$$E_2 - E_1 = \frac{e^4 m_e}{(4\pi\varepsilon_0)^2 2\hbar^2}\left(\frac{1}{n_1^2} - \frac{1}{n_2^2}\right), \tag{2.3}$$

where the Plank relation $E\lambda = hc$ allows to directly relate this equation to the Rydberg formula 2.2 from above. One finds [25]

$$R_\infty = \frac{e^4 m_e}{8\varepsilon^2 h^3 c} = 1.09737 \times 10^7 \text{ m}^{-1} \approx R_H \ , \tag{2.4}$$

where R_∞ indicates that in the derivation of this relation the mass of the nucleus of the atom was assumed to be infinitely large. Nevertheless, this value agrees very well with the empirically found value R_H and can indeed be considered as a milestone in physics.
Another important result of the Bohr model is its prediction about the radius of the electron's orbit, which shows the importance of Rydberg atoms. Due to the quantization only certain radii are allowed and are given by:

$$r_n = \frac{4\pi\varepsilon_0 n^2 \hbar^2}{e^2 m_e} \tag{2.5}$$

Even though the assumption of circular orbits of the electron is oversimplified, the Bohr model correctly predicts that the radius scales quadratically in n, which is of great importance for the exaggerated properties of highly excited Rydberg atoms. An electron in the $n = 10$ state is on average 100 times further away from the ionic core than an electron in the ground state. The binding energy for example of such an electron will substantially be reduced, while the dipole moment of the atom will strongly be enhanced. Evidently, such atoms will show interesting properties which are worth studying.

2.2. Wavefunction of Rydberg atoms

The goal of this section is to derive and highlight some of the properties of Rydberg atoms and to go beyond the Bohr model described above. Despite its nice simplicity, the model can explain surprisingly well some of the basic properties of the hydrogen atom, but fails when it comes to more subtle effects. For a thorough discussion of the hydrogen atom one needs to know its wavefunction and the starting point for this is the Schrödinger equation.
At this point it is convenient to introduce atomic units, which are chosen such that all relevant parameters are in units of the corresponding hydrogen ground state parameter. The unit of the mass for example is switched from kilogram to the mass of an electron and the length from meter to the radius of the first Bohr radius. For a table of the most important units see Tab. A.1.

2.2.1. Solution in spherical coordinates

The Schrödinger equation for the wavefunction of an electron in a hydrogen atom in atomic units is given by [23]

$$H\psi = \left(-\frac{\nabla^2}{2} - \frac{1}{r}\right)\psi = E\psi \,, \tag{2.6}$$

where H is the Hamilton operator, r the electron's distance from the core and E is its energy. Here the mass of the core is assumed to be infinite, which is a common approximation. To solve this equation one can use the spherical symmetry of the problem, which suggest to employ a separation ansatz, i.e. to write the wavefuncion as product of the angular and the radial component. The solution in spherical coordinates is then given by [26]

$$\psi_{nlm}(r,\theta,\varphi) = |nlm\rangle = R_{nl}(r)Y_{lm}(\theta,\varphi)\,, \tag{2.7}$$

with the well known principal quantum number n, the orbital quantum number l and the magnetic quantum number m. R_{nl} are the radial wavefunctions of the hydrogen atom and Y_{lm} the spherical harmonics. A detailed derivation of this solution, as well as an analytical expression for the wavefunctions, can be found for example in Ref. [25] or in any textbook on quantum mechanics.

An important result of the quantum mechanical treatment of the hydrogen atom is the quantization of the energy levels given by:

$$E_{nlm} = -\frac{1}{2n^2} \tag{2.8}$$

The energy depends only on the principal quantum number n and each energy level shows a degeneracy of n^2.

The wavefunction $\psi_{nlm}(r,\theta,\varphi)$ of the electron of the hydrogen atom allows to calculate the expectation value of any operator and to derive important scaling laws. Of particular interest for Rydberg atoms is the expectation value of the distance between electron and nucleus [23]

$$\langle r\rangle = \frac{1}{2}\left[3n^2 - l\,(l+1)\right]. \tag{2.9}$$

As the orbital quantum number l can take values only up to $l = n-1$, the expectation value increases faster than $\frac{1}{2}\left[2n^2+n\right]$. A list of some quantities of interest with their scaling law for large n is given in the table 2.1 below.

Property	n dependence
Binding energy	n^{-2}
Orbital radius	n^2
Energy between adjacent n states	n^{-3}
Dipole moment	n^2
Radiative lifetime	n^3

Table 2.1.: Scaling laws for different quantities of highly excited Rydberg atoms [23].

So far only the case of the hydrogen atom was discussed, but the term 'Rydberg state' is used for any atom or even for molecules [26] excited to states with a high principal quantum number n. If one considers for example the Na atom excited to a Rydberg state, the difference is that the ionic core Na^+ now consists of eleven protons and ten electrons. As the average distance of the electron to the core is around two orders of magnitude larger than the core itself, it is reasonable to assume that the properties of all Rydberg atoms are similar.
If the electron is in a high l-state it rarely comes close enough to the center, such that the ionic core can be approximated by a point charge, as in was done for the hydrogen atom [23]. However, if the Rydberg electron comes close to the core region, the exact charge distribution becomes important. The electron can polarize or even penetrate the Na^+ core, which both increases its binding energy [23]. These effects are usually only relevant for states of low orbital angular momentum.

2.2.2. Linear Stark effect

In the previous section the Schrödinger equation for the hydrogen system was solved in spherical coordinates. Due to the spherical symmetry of the electric field of the proton in the hydrogen atom, it was possible to separate the variables and to find analytical expressions for all the eigenfunctions $|nlm\rangle$.
Of particular interest for the following chapters is the question, how an external homogeneous electric field $\vec{F} = (0, 0, F)$, where $F = |F|$, alters the energy levels of the hydrogen atom. The field is assumed to be small enough to be treated as perturbation. This new system is described by the Hamiltonian operator

$$H = H_0 + Fz = H_0 + Fr\cos\theta \,, \tag{2.10}$$

where H_0 is the Hamiltonian of the unperturbed hydrogen atom, see Eq. 2.6. In the second equation the z coordinate is expressed in spherical coordinates. The perturbation matrix elements $\langle n'l'm' \,|Frcos\theta|\, nlm\rangle$ can be written as a product of an angular and radial part,

$$F \left\langle n'l' \,|r|\, nl \right\rangle \left\langle l'm' \,|\cos\theta|\, lm \right\rangle \,. \tag{2.11}$$

Furthermore, the characteristic symmetry properties of the spherical harmonics allow to derive selection rules for this electric dipole interaction given by

$$\Delta m = 0 \quad \Delta l = \pm 1 \quad \Delta n = 0, \pm 1, \pm 2, ... \tag{2.12}$$

One immediate result of this perturbation analysis is that the l degeneracy of the states with the same quantum number n is lifted, a consequence of the broken spherical symmetry. Another important result is a linear Stark shift, which modifies the energies of the states proportional to the electric field strength F. This follows from the linear F dependence of the off diagonal elements in the perturbation matrix, which implies that its eigenvalues are

proportional to F as well [23].
To find new eigenfunctions, which ideally diagonalize the full Hamiltonian, one starts from the eigenfunctions of the unperturbed system. The ansatz for the perturbation expansion is that the solutions for the new eigenstates $|n\rangle$ and the new eigenvalues E_n can be written as [27]

$$E_n = E_n^0 + FE_n^1 + F^2E_n^2 + ... \tag{2.13}$$

$$|n\rangle = \left|n^0\right\rangle + F\left|n^1\right\rangle + F^2\left|n^2\right\rangle + ... \tag{2.14}$$

where F is the perturbation parameter which in this case is the electric field. The first term in the expansion comes from the unperturbed system and the superscript indicates the order of the expansion. In general this is an infinite series which does not necessarily converge, but in many cases it is sufficient to consider only terms up to first or second order. The analytical solution of the unperturbed system of the hydrogen atom in Eq. 2.7 could in principal be used for this calculation. This would however be quite difficult to do for the following reason. The states of the same quantum number n in the unperturbed system are degenerate and, even worse, the perturbation term Fz mixes those states as it is shown in Eq. 2.12. The consequence is that perturbation theory for degenerate states must be used, and hence for each energy level a basis needs to be found which diagonalizes the perturbation matrix [27] in the subspace of this energy level.
A convenient way to circumvent this problem is to use parabolic coordinates for the quantization of the hydrogen atom [28]. The problem remains separable and in particular the eigenfunctions diagonalize the perturbation matrix which facilitates calculations.

2.3. Solution in parabolic coordinates

The optimal choice of the coordinate system is closely related to the symmetry of the problem to solve. For the unperturbed hydrogen atom spherical coordinates are appropriate, but for problems where a specific direction is distinguished, parabolic coordinates are a better choice [28]. The parabolic coordinates ξ , η and φ are defined by the relations

$$x = \sqrt{\xi\eta}\cos\varphi, \quad y = \sqrt{\xi\eta}\sin\varphi, \quad z = \frac{1}{2}(\xi - \eta) \tag{2.15}$$

$$r = \sqrt{x^2 + y^2 + z^2} = \frac{1}{2}(\xi + \eta) \tag{2.16}$$

and inversely by (2.17)

$$\xi = r + z \quad \eta = r - z \quad \varphi = \arctan\frac{y}{x}\,. \tag{2.18}$$

By writing the unperturbed Schrödinger equation in parabolic coordinates and making the separation ansatz $\Psi = f_1(\xi)\, f_2(\eta)\, e^{im\varphi}$, it is again possible to find analytical expressions for the eigenfunctions. A detailed derivation can be found in [28]. The functions are given by

$$|n_1 n_2 m\rangle = \Psi_{n_1 n_2 m}(\xi, \eta, \varphi) = \frac{\sqrt{2}}{n^2} f_{n_1 m}\left(\frac{\xi}{n}\right) f_{n_2 m}\left(\frac{\eta}{n}\right) \frac{e^{im\varphi}}{\sqrt{2\pi}} \tag{2.19}$$

with

$$f_{pm}(\rho) = \frac{1}{|m|!}\sqrt{\frac{(p+|m|)!}{p!}} F(-p, |m|+1, \rho)\, e^{-\rho/2} \rho^{|m|/2} , \tag{2.20}$$

where $F(\alpha, \gamma, z)$ is the confluent hypergeometric function [28]. Here it is good to know that if α is a negative and γ a positive integer, then this function is a polynomial of order $|\alpha|$ and is equivalent to the generalized Laguerre polynomials $L^{\gamma}_{|\alpha|}$ up to a constant factor.
In parabolic coordinates, every stationary state is fully described by the two nonnegative parabolic quantum numbers n_1 and n_2 and the magnetic quantum number m. The principal quantum number n is given by the relation

$$n = n_1 + n_2 + |m| + 1 , \tag{2.21}$$

which determines the allowed quantum numbers. By counting all possible combinations of n_1, n_2 and m one finds a degeneracy of n^2 which agrees with the previously found results for the eigenstates in spherical coordinates. The parabolic state $|n_1 n_2 m\rangle$ with principle quantum number n can be written as a superposition of these states like [23]

$$|n; n_1 n_2 m\rangle = \sum_l \langle nlm | n_1 n_2 m\rangle\, |nlm\rangle \ . \tag{2.22}$$

It follows that its energy is again given by $E_n = -\frac{1}{2n^2}$.

2.3.1. The Hydrogen atom in an electric field

The reason why parabolic coordinates are introduced, was the observation, that the eigenfunctions in spherical coordinates are not optimal to describe a hydrogen atom in a weak electric field along the z - axis. While these wavefunctions are symmetric about the z = 0 plane, the parabolic eigenfunctions are asymmetric about it. The argument why this asymmetry is useful, is that an external field $\vec{F} = (0, 0, F)$ leads to different potential energies for an electron with a positive and negative z value.
A convenient measure for this asymmetry in parabolic coordinates is given by the quantum number $k = n_1 - n_2$, where the allowed values for k are defined by the relation 2.21. For $k > 0$ the density distribution is larger on the side with $z > 0$, and for $k < 0$ the contrary holds. This effect is shown in Fig. 2.1, where the density distribution $|\psi|^2$ for the eigenstates with $n = 8$, $m = 0$ and different k values is plotted in the x-z plane. One can clearly see the that for positive k the electrons are dominantly found along the positive z - axis, and vice

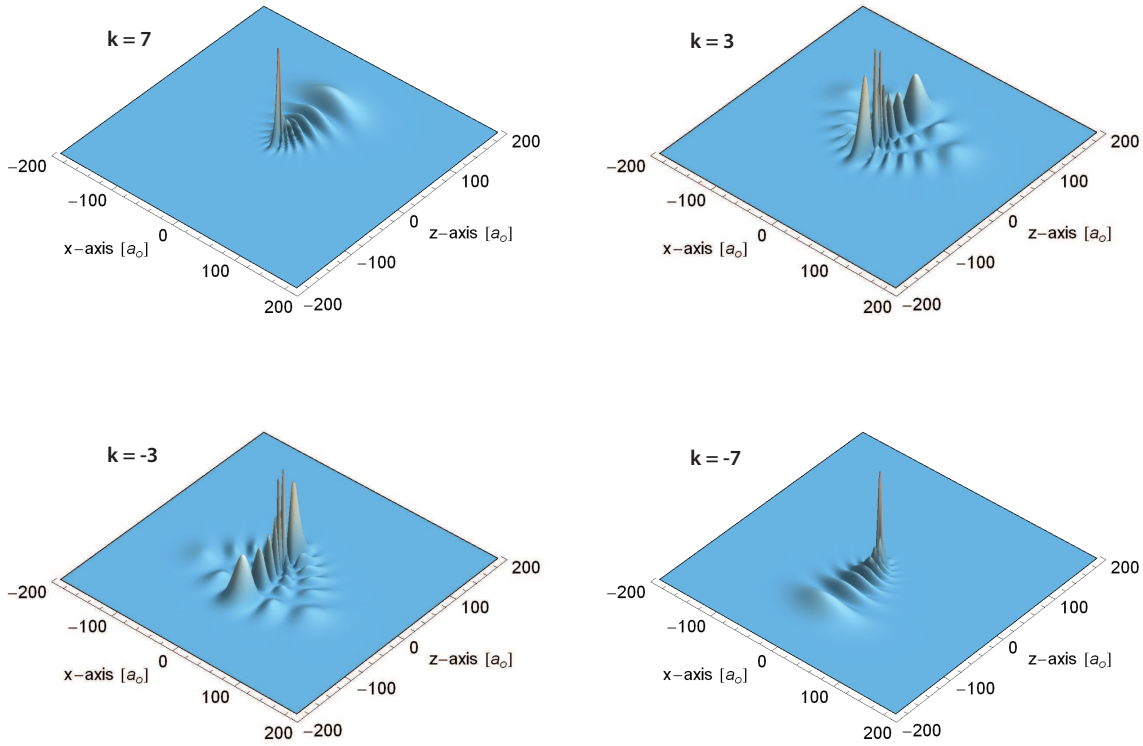

Figure 2.1.: The four plots show the probability density distribution $|\psi|^2$ of the parabolic eigenfunctions with $n = 8$ and $m = 0$ for different values of the k quantum number in the x-z plane. There is no applied electric field, such that the quantization axis z can be chosen arbitrarily. For positive k the electron is preferably along the positive z-axis. The effect is more pronounced for higher k. The distribution for negative k values are given by a mirroring about the $z = 0$ plane

versa for negative k[1].

From these figures it is apparent that for larger values of $|k|$, the electrons are on average further away from the $z = 0$ plane. This characteristic will lead to a splitting of the energies of the k states if an electric field $\vec{F} = (0, 0, F)$ is applied.

This energy shift for the parabolic eigenstates is calculated with perturbation theory and the first order correction is given by [28]

$$E^{(1)} = \frac{3}{2} F n k \,, \tag{2.23}$$

where F is the electric field strength defining the z - axis and n is the principal quantum number. The energy of the state $|n_1 n_1 m\rangle$ is thus given by

[1] It is a bit unfortunate that the plots are dominated by the large, but finite and narrow peak close to the origin. However, the integration over the whole space shows that its contribution for large n is actually negligible. The figures of the density distribution of the same eigenstates in reference [23] or [22] are scaled by r^2, which is justified by an 'improved visibility'. Those plots look more instructive, but no longer show the correct distribution in the x-z plane. Therefore this scaling was skipped here.

$$E_{n_1 n_2 m} = -\frac{1}{2n^2} + \frac{3}{2}Fnk \; . \tag{2.24}$$

The first term is the binding energy of the electron in the unperturbed system, as it is given in Eq. 2.8. The linear field dependence of the energy shift was previously obtained by the perturbation matrix in spherical coordinates. The important advantage of parabolic coordinates is now, that states of equal quantum number n are not mixed by the applied field, since the perturbation matrix in parabolic coordinates is diagonal in this subspace. To calculate the new eigenfunctions of the problem, one has to consider only additional terms in the expansion 2.14 originating from the coupling to levels of different n. These contributions are proportional to $\frac{1}{\Delta E}$, where ΔE is the energy difference between those levels [27].
Fig. 2.2 shows this linear splitting of the energy for the $n = 4$ level in an electric field in arbitrary units. The allowed combinations of the quantum numbers m, n_1 and n_2 for a given n are given by Eq. 2.21 and are indicated in the figure. If n and m are fixed, then

$$n_1 = 0, 1, 2, ..., n - |m| - 1 \tag{2.25}$$

$$n_2 = n - |m| - 1, n - |m| - 2, ..., 1, 0 \; , \tag{2.26}$$

from which follows that $k = n_1 - n_2$ can take values ranging from $-n + |m| + 1$ to $n - |m| - 1$ in steps of two. Therefore there are $n - |m|$ such levels and each of them shows a $(n - |k|)$ - fold degeneracy.
States with lower energy in an applied electric field ($k < 0$) are commonly referred to 'red-shifted' or 'high-field seeking' states, and to 'blue-shifted' or 'low-field' seeking states ($k > 0$) if their energy is increased, respectively. This is a very instructive notion and will be used throughout this thesis, as it is related to the energy of the Rydberg atom in the electric field. In Fig. 2.2 the calculated energy levels of all Stark states in the hydrogen atom from $n = 6$ to $n = 8$ are plotted versus the applied electric field strength. One can see that if the field reaches a certain threshold, the most blue-shifted state crosses the most red-shifted state of the next higher n level. The field strength at which this occurs is called Inglis-Teller field and is given by [23]

$$F_{IT} = \frac{1}{3n^5} \; , \tag{2.27}$$

where n is the principal quantum number of the blue-shifted state. In case of the hydrogen atom, these two states are exactly degenerate at the crossing. The reason for this is an additional symmetry of the coulomb potential, resulting in a constant of motion in the classical description (Runge-Lenz vector) and in an operator which commutes with the Hamiltonian in quantum mechanism, leading to an extra degeneracy [28]. In the hydrogen atom this operator has different eigenvalues for the two states, allowing them to cross.
However, in non-hydrogenic atoms the potential deviates from the perfect coulomb potential, leading to an interaction between the different Stark states and the crossing between them

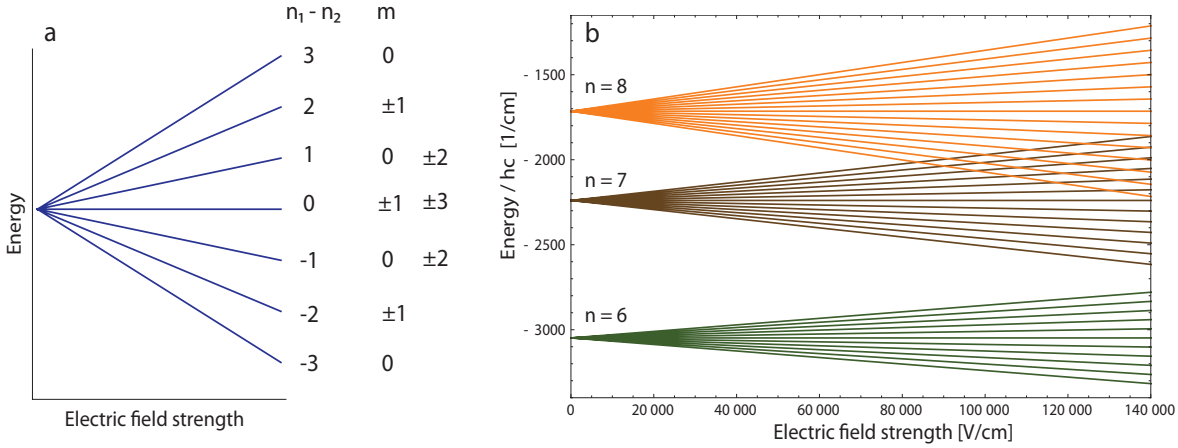

Figure 2.2.: (a) The linear Stark effect in the hydrogen atom for $n = 4$ in arbitrary units. The energies of all Stark states are plotted vs. the electric field and for each $k = n_1 - n_2$ value, the allowed magnetic quantum number m is given. (b) All hydrogenic Stark states from $n = 6$ to $n = 8$ are plotted. Above a certain field strength, known as Inglis-Teller field, Stark states with different n start to cross. For hydrogen atom, these crossings are not avoided.

becomes avoided [29]. This effect then limits the electric field that can be applied in some experiments [30].

2.4. Field ionization of Rydberg atoms

Field ionization of Rydberg states is an important tool for various experiments as it enables to determine both the position [31, 21], as well as the state of the Rydberg atom [23, 26]. The required field to ionize an atom in is ground state is fairly large, but decreases rapidly with increasing n, which facilitates the experiments.
There is an instructive method to estimate the ionization field for Rydberg states. The potential energy of the hydrogen's electron in an external field is given by

$$V = -\frac{1}{r} + Fz \,, \tag{2.28}$$

which was previously used in Eq. 2.6 and 2.10. The location of the saddle point of this potential along the z - axis is found by setting $\frac{\partial V}{\partial z} = 0$ and is given by $z = -\frac{1}{\sqrt{F}}$, where the value of the potential is $V = -2\sqrt{F}$. By assuming that the electron is in the most red-shifted state, such that $n \approx -k$, then the classical condition for the ionization is [29]

$$E = -\frac{1}{2n^2} - \frac{3n^2 F}{2} = -2\sqrt{F} \,, \tag{2.29}$$

which follows from Eq. 2.24. Using this equation one finds a threshold field of

$$F_{ion}^{red} = \frac{1}{9n^4} \,. \tag{2.30}$$

The ionization field for the most blue-shifted state will be about twice as large as the one calculated here for the most red-shifted state [29]. For the blue-shifted states ($k > 0$) the probability distribution is highest for positive z values, as it is shown in Fig. 2.1. On the other hand, the saddle point is located at the negative side of the ion core, which makes it less likely for the atom to be ionized. This qualitatively explains why a higher ionization field is required for the blue-shifted states.
This characteristic allows not only to gain information about the principal quantum number n, but also about the Stark state of an atom by applying electric fields of different magnitude, which is explained in more detail in Section 3.3.
As quantum mechanics is not deterministic, this process is described by the probability that an atom is ionized within a certain time interval for a given electric field . An approximation of this rate for the hydrogen atom is given in [32]. It is useful to note, that this rapidly increases to rates of $10^6\ \mathrm{s}^{-1}$ to $10^9\ \mathrm{s}^{-1}$ over a very narrow field range above the ionization limit [26].

2.5. Lifetime of Rydberg states

An important requirement for experiments conducted with Rydberg atoms is that the duration of an experimental cycle does not exceed the lifetime of the state of interest. For Rydberg atoms in an electric field well below the ionization limit, this time is determined by the spontaneous decay and by black body radiation induced transitions. At a finite temperature T, it is given by [23]

$$\frac{1}{\tau_T} = \frac{1}{\tau} + \frac{1}{\tau_{bb}}, \tag{2.31}$$

where τ is the lifetime at 0 K and τ_{bb}^{-1} the decay rate due to black body radiation.

Spontaneous emission

The spontaneous decay rate from the energy level with quantum number n to a lower lying level n' is characterized by the Einstein A coefficient, for which in the field free case [23]

$$A_{n'l',nl} \propto \omega_{n'l',nl}^3 \left|\langle n'l' |r| nl\rangle\right|^2 \tag{2.32}$$

holds, where $\omega_{n'l',nl}$ is proportional to the energy difference between the states $|nl\rangle$ and $|n'l'\rangle$. The scaling with ω^3 generally implies that the decay into the ground state dominates this process, if the transition is allowed. This leads to another important conclusion for low-l states. As for states $n' \to \infty$ the transition frequency ω to the ground state approaches a constant value, the decay rate essentially depends on the overlap of the two wavefunctions. The amplitude of the wavefunction $|n'l'\rangle$ in the immediate vicinity of the core region scales

like $n^{-\frac{3}{2}}$ [26], which implies that the decay rate $A_{n'l',nl}$ scales like n^{-3} and therefore the lifetime with n^3.
The lifetime of Stark states with a high principal quantum number n scales even like n^4. The reason for this difference is that the Stark state is a superposition of different l states, as shown in Eq. 2.22, and that the decay rate for high-l states is suppressed. This leads to radiative lifetimes for Stark states with $n \approx 20$ of several tens of microseconds [29].

Black body radiation induced transitions

Rydberg atoms are very sensitive to black body radiation, even at room temperature. The lifetime limited by black body radiation τ_{bb} scales like n^{-2}, which is slower than the scaling of the spontaneous decay rate [29]. There are mainly two reasons for this. For high quantum numbers n the energy separation between adjacent levels is small, as this difference scales like n^{-3}, see Tab. 2.1. The second reason is that the dipole transition rates between Rydberg states is large, which strongly couples them to the radiation field.
The black body radiation field can be characterized by the number of photons per mode of the radiation field. This photon occupation number $\bar{n}$ is given by [29]

$$\bar{n} = \frac{1}{e^{\frac{h\nu}{kT}} - 1} \,, \tag{2.33}$$

which is reduced to $\bar{n} \cong \frac{kT}{h\nu}$ if $h\nu \ll kT$ holds. From this relation one can draw an interesting conclusion. Black body radiation at frequencies higher than $\frac{kT}{h\bar{n}}$, where $\bar{n} \ll 1$, can be neglected, because the vacuum fluctuations are given by $\bar{n} = \frac{1}{2}$ [23]. In this regime the spontaneous emission is dominant, which is based on those vacuum fluctuations. However, if $\bar{n} \approx 10$, transition rates induced by black body radiation between Rydberg states can be larger by an order of magnitude compared to the rates of spontaneous emission [23].
Another difference to the spontaneous emission is that these transitions are preferably between neighbouring n levels, due to the small energy gap and the high photon occupation number of the black body radiation field at low frequencies. From Fig. 2.1 it is as well apparent that transitions to states of similar k values are favored, as their wave function overlap is largest. Black body radiation therefore leads to a mixture of states among the initial values of n and k. At room temperature this happens on the timescale of 20 μs for Rydberg states with $n = 20$ [29].
The relevant parts of the experiment, which is discussed in the subsequent chapters and illustrated in Fig. 3.1, is cooled to 4 K. This will drastically reduce the radiation from the background, such that the effect of the black body radiation is assumed to be negligible [33]. In this environment, the lifetime of a $n = 30$ and $k = 25$ Stark state of the hydrogen atom – similar states will be used in the experiment – is expected to be close to the fluorescence lifetime of 135 μs determined in a recent experiment [21]. This obtained lifetime is mainly limited by the spontaneous decay [33], as it will be the case in the current experiment.

2.6. Acceleration of Rydberg atoms in inhomogeneous electric fields

Rydberg atoms in an inhomogeneous electric field are subject to a force based on the linear electric field dependence of the energies of Stark states, as given in Eq. 2.24. This relation was derived by first order perturbation theory and the force acting on the Rydberg atom can be calculated by taking the negative gradient of the potential energy [29]:

$$\vec{f} = -\nabla E_{Stark} = -\frac{3}{2} nk \nabla F = -|\mu| \nabla F \tag{2.34}$$

Here $|\mu| = \frac{3}{2}nk$ is the dipole moment of these atoms. Due to the huge separation between the core and the valence electron in highly excited Rydberg atoms, this dipole moment can exceed naturally occurring dipoles in polar molecules by several orders of magnitude [30].
These special property gave rise to experiments aiming to decelerate atoms or molecules in order to obtain a ensemble of ultra cold particles to perform high resolution spectroscopy for example[30]. In these experiments, a beam of atoms with ideally zero transverse velocity propagates along the z - axis and is excited to a Rydberg Stark state. If the z - component of ∇F is nonzero, then the beam is either accelerated or decelerated, depending of the Stark state. For $\partial_z F < 0$ the blue-shifted states ($k > 0$) are accelerated and the red-shifted ($k < 0$) states decelerated. For $\partial_z F < 0$ it would be reverse. Assuming static fields, one can calculate the change in the kinetic energy [29]

$$\Delta E_{kin} = -\frac{3}{2} nk \left(F\left(z_f\right) - F\left(z_i\right)\right) = -\frac{3}{2} nk \Delta F. \tag{2.35}$$

In such an experiment [30] Argon atoms in a homogeneous electric field of 367 V/cm are excited to the $k = -21$ and $n = 22$ state, therefore the most red-shifted Stark state. By using Eq. 2.35 one finds a maximum change in the kinetic energy of 2.15×10^{-22}J which corresponds to a deceleration of 80 m/s compared to the initial velocity 588 m/s. A problem of this deceleration scheme is that the electric field cannot be increased arbitrarily, as it would be suggested by Eq. 2.35. The maximal applied electric field is limited by the avoided crossings between different Stark states, occurring at a field strength above the Inglis-Teller limit. However, by applying time dependent fields the deceleration can be improved, as explained and demonstrated in Ref. [29, 30, 21]
Equation 2.35 for the change in the kinetic energy does not depend on the specific atom. It follows that the lighter hydrogen atoms are far easier to decelerate than Argon atoms. This enabled to stop hydrogen atoms and to load them into a two [34] or three dimensional trap [21], respectively. The trapping is achieved by a quadrupole configuration of the electrodes, resulting in a field minimum in the center. For blue-shifted Rydberg states this results in a potential minimum, and the field gradients generate forces that confine these Rydberg atoms. This experimental setup will be discussed in more detail in Section 4.5.1.

3. Experimental Setup

The experimental setup is partially based on previous designs for the deceleration and the electrostatic trapping of Rydberg atoms [35, 21, 29] and is illustrated in Fig. 3.1. A supersonic beam of hydrogen atoms propagates along the main axis, which is either called z-axis or beam axis throughout this thesis. Four parallel cylindrical electrodes are placed along this axis. Between the first pair, the excitation region, laser radiation will excite the hydrogen atoms to a Rydberg state with a specific n and k value. In the second stage, the atom beam will traverse an atom chip. Between the third and last electrode, the ionization region, a large voltage pulse field - ionizes the atoms and accelerates them towards the multichannel plate (MCP) detector. The whole experiment is conducted in vacuum.
As an extension of previous setups for the deceleration of Rydberg atoms [30, 21], in the new design all relevant parts of the experiment are cooled down to a temperature of 4 K with a pulse-tube cooler. This enables to investigate the interaction between Rydberg atoms and on-chip superconducting microwave resonators, which is of particular interest, as such resonators are used for solid state based qubit implementations [36].

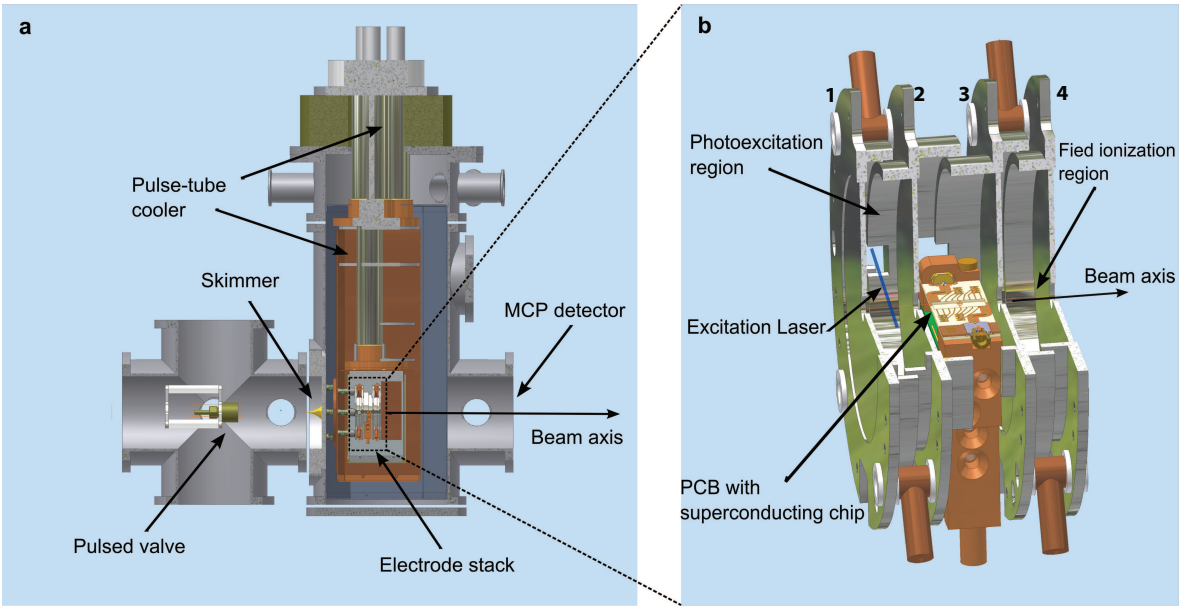

Figure 3.1.: (a) Cross section of the experimental setup with the vacuum chamber, the pulse tube-tube cooler and the indicated MCP detector. The atom cloud is generated by the pulsed valve and the skimmer, see Section 3.1. (b) Enlarged view of the electrode stack. The different regions are labeled and the electrodes are numbered according to the description in the text.

3.1. Supersonic gas beam

A supersonic gas beam can be generated by passing a gas through a pulsed valve into vacuum [29]. There the gas will expand adiabatically and at a certain distance along the z-axis, the gas passes a skimmer into a second vacuum chamber. In this way a gas sample is generated with a low transverse kinetic energy, as explained in detail in Ref. [37]. The spread Δv around the mean velocity is assumed to follow a normal distribution and can be related to a temperature by $m/2\,(\Delta v)^2 = k_B T$, where k_B is the Boltzmann constant. A schematic figure of this process is shown in Fig. 3.2.

In the experiment, the initial gas is a mixture of NH_3 seeded in a rare gas. The reason of this seeding is to lower the average velocity of the particles of interest. In fact, the Maxwell Boltzmann distribution predicts a mean velocity that is proportional to $\frac{1}{\sqrt{m}}$ of the gas particles with mass m . Therefore the heavier the particle, the lower is the mean velocity at a given temperature. The idea is now, that by collisions of NH_3 with heavier atoms, the mean velocity of the gas of interest can be pushed below the mean velocity predicted by the Maxwell Boltzmann distribution at a given temperature.

Another, actually more important reason, is to avoid that the NH_3 molecules stick together [33]. The initial gas mixture consists of approximately 90 % rare gas, which ensures a homogeneous distribution of the NH_3 molecules.

The ground state hydrogen atoms are generated by excimer laser photolysis of NH_3 [34]. This laser radiation is applied between the pulsed valve and the skimmer.

In the excitation region between electrode 1 and 2, see Fig. 3.1, two counterpropagating laser beam cross the atom beam. Vacuum-ultraviolet (VUV) laser radiation drives the transition between the hydrogen ground state and the intermediate $2\,^2$P state. UV laser radiation subsequently excites the atom to a specific Rydberg Stark state in the range of $n = 20$ to $n = 35$. This resonant two-photon transition is schematically illustrated in Fig. 3.2.

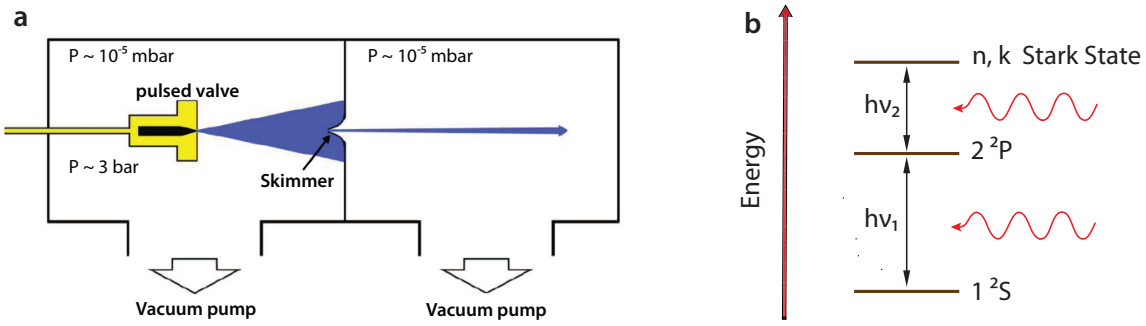

Figure 3.2.: (a) Schematic drawing of the process to generate a supersonic beam. The gas with a pressure of $P_0 \approx 3$bar is initially passed through a pulsed valve into vacuum, where it expands adiabatically before it traverses a skimmer with an opening of 5 mm. This procedure allows to select the translationally coldest particles. (b) Resonant two-photon to a Rydberg stark state with quantum numbers n and k via the intermediate $2\,^2P$ state. ν_1 is in the VUV and ν_2 in the UV range.

3.2. Electrode stack

The electric field in the excitation and the ionization region is generated by a set of four electrodes. The different stages are schematically drawn in Fig. 3.3.

In the excitation region an electric field of around around 100 V/cm will be applied such

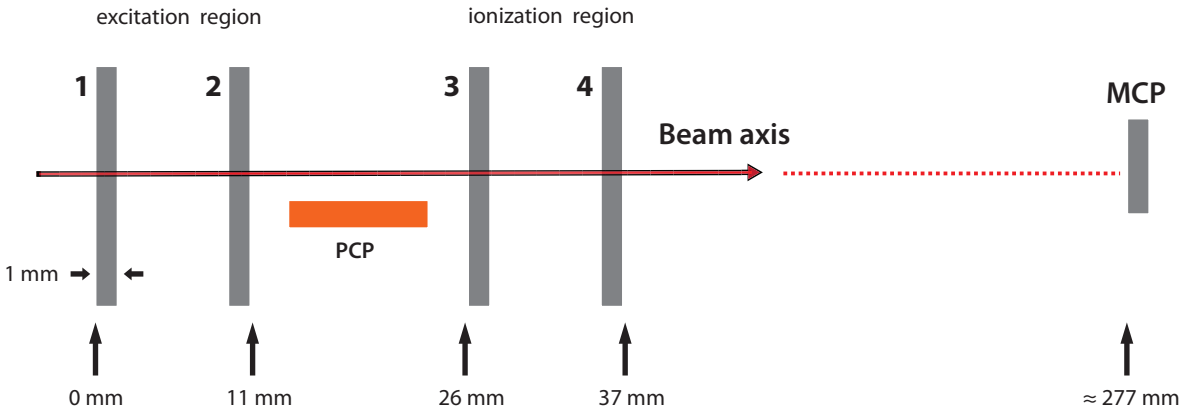

Figure 3.3.: Schematic assembly of the stack electrodes along with relevant length scales. The beam passes the cylindrical electrodes through an opening in the center. The atoms are excited between the first and second electrode before they cross the printed circuit board (PCB) in the center region. After the atoms are ionized between the third and fourth electrode, they are accelerated towards the MCP.

that the different Stark states are sufficiently separated and therefore accessible by the laser radiation. The bandwidth of the excitation laser is 0.008 cm^{-1} [29][1] and the energy separation between two adjacent Stark states with principal quantum number $n = 30$ is 0.384 cm^{-1} in an electric field of 100 V/cm. In addition, the field must be lower than the Inglis-Teller field. Further more, the electric field seen by the atoms should not drop below around 10 V/cm [33], in order to ensure a quantization axis for Stark states along the entire beam axis [21]. In this experiment it is not intended to decelerate the atoms. Therefore, one would preferably have a homogeneous electric field along the beam axis, but here this is not a strict requirement. The quantization axis z of the atom follows the changing field direction, as long as this change is slow compared to the transition frequency between adjacent Stark states [38]. As in this experiment the atoms are slow and the applied fields are static or only slowly varying, the evolution of the electric field seen by the atoms can be considered to be adiabatic and the Stark state to be preserved.

3.2.1. Electric field simulations

Close to the atom chip in the region between the second and the third electrode, it will be difficult to maintain the original field strength. As the chip is connected to ground, its surface

[1] Numerical values of the energy are commonly given in units of $\frac{1}{cm}$. The conversion to standard units is given by the relation $E[cm^{-1}] = E[J] \cdot hc$

will be on an equipotential surface and the electric field close to the PCB is reduced.
To illustrate this, the magnitude of the electric field is shown in Fig. 3.4 for different uniform materials of the PCB. Using a finite element program[2], it is possible to calculate the electric fields at the position of the atom beam for different sample materials and potential configurations.
For a copper sample, the electric field strength above the surface is substantially reduced, as expected. The large peak in Fig. 3.4 (b) is due to the potential difference between electrode and chip, combined with the relatively short separation of 2 mm. To remove this peak the applied potentials were adjusted in plot (c). However, by applying time dependent potentials on the electrodes in the experiment, it should be possible to account for these effects. The idea is to optimize the electric field at the instantaneous position of the atom cloud along the axis. This means that while the atoms are right above the chip, large potentials can be applied to maintain a certain field strength. In the same way the fluctuations in the electric field seen by the atoms can be reduced.
If no sample is inserted, see Fig. 3.4 (a), the field strength is constant in between the electrodes, while showing a slight decline at the crossing of the electrodes. However, this should not be an issue for the stability of the internal state of the Rydberg atoms [33].
Fig. 3.4 (d) shows the result if a dielectric medium[3] is placed at the position of the PCP. The peaks of the electric field strength between the electrodes and the sample are observed similar to the case of the copper sample, though their amplitude is lower and in between the electrodes the field is homogeneous.

3.2.2. Field ionization region

In the ionization region, a large voltage pulse on the third electrode is applied in order to ionize the atoms and to accelerate the ions in positive z direction towards the MCP detector. Using Eq. 2.30 the required ionization fields can be calculated. For Rydberg states in the range of $n = 30$ and a k value around 25, the ionization field for such a blue-shifted state can be estimated:

$$F_{ion}\left[\frac{V}{cm}\right] = 2\,\frac{1}{9n^4}\,C = 2\,\frac{1}{9\cdot 30^4}\cdot 5.14\times 10^9\,\frac{V}{cm} = 1.41\times 10^3\frac{V}{cm}\,. \tag{3.1}$$

C in the second equation is the conversion factor from atomic to standard units, given in Tab. A.1. For a separation between the two electrodes of 9 mm the required voltage difference is around 1.3 kV. If state selective ionization is required, it is important to precisely control the amplitude of the applied pulse. As the rise time should be short[4] it is important to consider unavoidable overshoot of the pulse amplitude as response to an applied square voltage pulse. Eventually, it is necessary to take the electric circuit properties of the electrodes and the cabling into account.

[2]For the simulation of the electric fields Maxwell Software was used, which will be discussed in Section 4.2.2.
[3]Here Arlon1000 is simulated. This material is used as dielectric in the PCBs which will be used.
[4]Currently a rise time of around 50 ns is anticipated

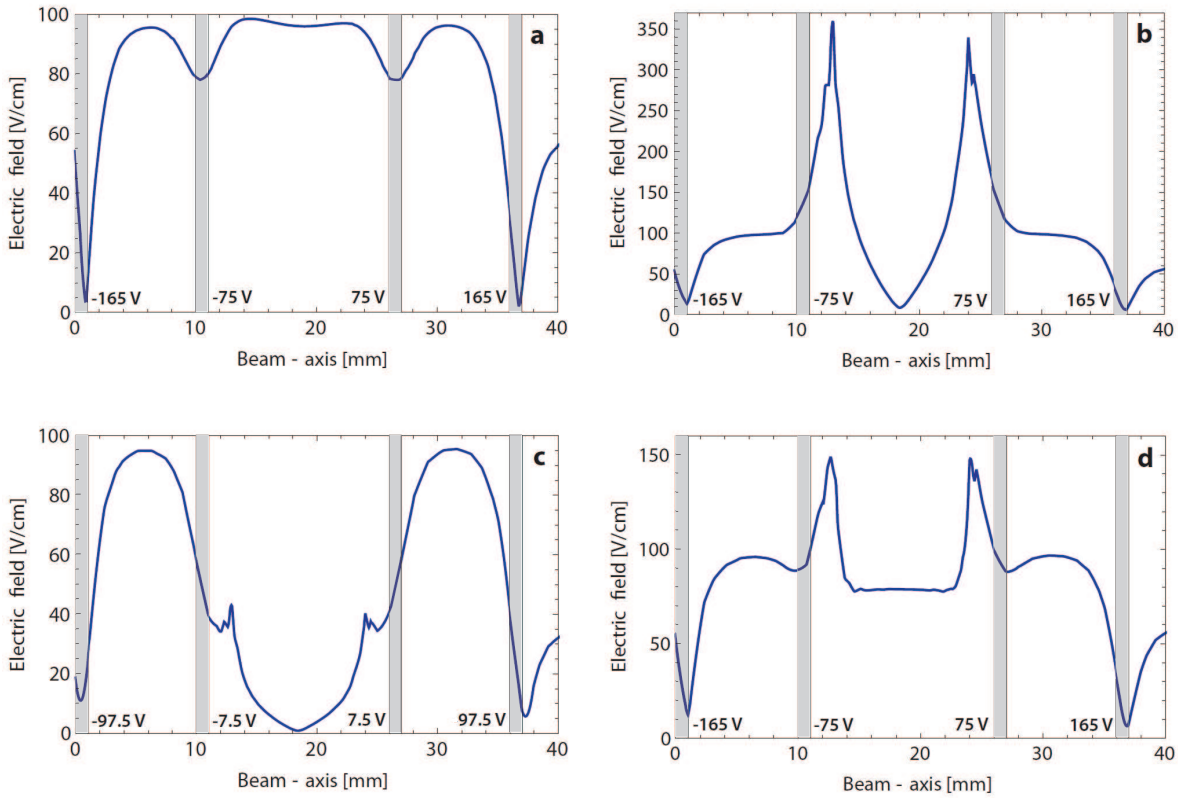

Figure 3.4.: Field strength along the beam axis and the distance is measured from the first electrode, see Fig. 3.3. The region of interest is from the excitation at 6 mm, to the ionization region at around 32 mm. The four black shaded rectangles indicate the location of the electrodes along the z - axis and next to each the applied voltage is displayed. Note the different scales in the plots for the field strength. Samples of different materials are used.(a) no sample is installed, (b) & (c) a copper plate connected to ground, with different applied potentials to the electrodes, (d) a plate of the dielectric Arlon1000.

3.3. Detection of atoms with a MCP detector

After field ionization of the Rydberg atoms in the last stage of the electrode stack, the ions are accelerated towards the MCP detector, where the impinging ions are recorded [39]. The MCP is used to reveal information both about the spatial as well as about internal Stark state distribution of the Rydberg atoms.

3.3.1. Spatial distribution

When an ion hits the MCP detector, its time of flight (TOF) will be recorded. This TOF spectra can be used to determine the z-position of the Rydberg atom right at the time of ionization, as with the knowledge of the field distribution and the arrival time, it is possible to trace the atom back to the initial position [34]. In addition, a phosphor screen can be mounted to the back of the MCP. The secondary electrons striking this screen induce a fluorescence signal and unveil the transverse spatial distribution, which can be recorded by a CCD camera [35].

3.3.2. Internal state spectroscopy

A careful analysis of the TOF spectra, combined with precisely applied ionization fields, is possible to draw conclusions about the distribution of the different Stark states among the ensemble of Rydberg atoms. This method makes use of the fact, that the ionization field for a Rydberg atom depends on the quantum numbers n and k. Therefore the field ionization is state selective [26]. By applying a ramped electric field at a specific slew rate, while recording the TOF, it is possible to reconstruct the internal state distribution. The Rydberg atoms are initially prepared in a well defined state. Therefore this method allows to detect perturbations of this state during the experimental cycle [22] like spontaneous decay or RF radiation induced transitions.

3.4. An on-chip quadrupole guide for Rydberg atoms

A source of such a RF - manipulation could be an on-chip resonator. It is an intermediate goal of this project to realize a coupling between the Rydberg atoms and a superconducting transmission line resonator, hence to demonstrate that these two different physical systems interact with each other. There are two different ways to observe this interaction.
The first one involves the change of the TOF spectra of the detected Rydberg atoms, as described above. A second approach, though less instructive, is to detect a state dependent change in the resonance frequency of the transmission line.
This dipole interaction is determined by the RF field generated by the transmission line and the internal state of the Rydberg atom. Due to the small two dimensional geometry of the

transmission line, the magnitude of the RF field will have a strong spatial dependence normal to the chip. To control the interaction strength it is therefore required, to regulate the exact position of the atom beam above the chip.
A strategy to achieve this level of control is to generate a potential minimum for certain Rydberg states above the transmission line by an on-chip quadrupole guide. This guide consists of four parallel wires, set to alternating voltages. For appropriately chosen potentials, this will lead to a minimum of the electric field strength above the surface, which generates a potential well for blue-shifted Stark states. The position of the minimum in the transverse plane can be adjusted by changing the applied voltages.
In the beginning of the experiment it is crucial to understand the individual components of the experiment precisely in order to gradually extend the range of applications along with the experimental complexity.
It is for example of particular importance to understand the effect of the surface of the chip on the Rydberg atoms. Due to their size, they exhibit a huge dipole moment and are very sensitive to electric fields. In a recent experiment [40], it was found that Rydberg atoms close to an atom chip show a distance dependent shift of the Rydberg energy levels, though a broadening of the levels was not observed. These shifts are expected to originate from a spatially inhomogeneous electric field generated by neutral adatoms deposited on the gold coated atom chip surface [41, 42].

3.4.1. Design

The aim of the quadrupole guide presented in this thesis is the guiding of Rydberg atoms across the PCB and as well the possibility to subsequently detect this effect with an MCP detector. For the first version it was decided to keep the electronic structures on the PCB sufficiently large, to allow an easy fabrication. This implies that the on-chip electrodes should be wider than around 300 μm.
Fig. 3.5 shows the drawing of the 34.8 mm $\times$ 11 mm PCB, which in the experiment is mounted to the sample holder, shown in Fig. 3.1. The atom beam crosses the PCB at the center along the short axis, as indicated in the figure by the red arrow.
The electrodes are aligned on the PCB such that they are parallel to the beam axis over the longest possible distance and are connected to the voltage source via circular pins. The connection to these pins at the end of the chip is symmetric about the beam axis in the vicinity of the center, ensuring that the electric quadrupole field lies parallel to the beam axis.
The electric field for this electrode configuration with applied voltages on the four PCB-electrodes of -40 V, 10 V, -10 V and 40 V is simulated in the transverse plane orthogonal to the beam axis. It is assumed that the electrodes are infinitely long, which yields reliable values at the center of the guide. The field strength in the plane exhibits a local minimum at a vertical distance of about 0.75 mm from the chip surface, as shown in Fig. 3.6. For the low-field seeking Stark states this corresponds to a potential minimum.

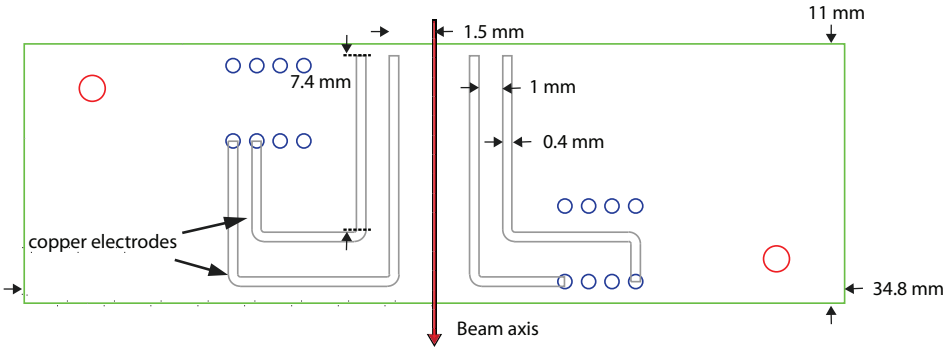

Figure 3.5.: Drawing of the quadrupole guide electrodes on the PCB. The red arrow indicates the propagation direction of the atom beam. The electrodes are parallel to the beam axis and are connected to the voltage source via circular pins.

3.4.2. Calculated properties of the Rydberg atom trap

The plots of the field strength through the field minimum in Fig. 3.6 (b) and (c) show that the applied potentials on the electrodes lead to a trap for blue - shifted Rydberg states in the transverse plane. As this confinement in x - and y - direction is ideally translational invariant along the beam axis, no forces are exerted in this direction, leading to a guide for the atom beam. Due to the inhomogeneous field, Rydberg atoms off the center axis of the guide experience a restoring force towards the center, which is given by

$$\vec{f} = -\frac{3}{2} nk \nabla F \,, \tag{3.2}$$

as described in Section 2.6. From Fig. 3.6 (b) and (c) it is apparent that the potential well is not harmonic, implying that the transverse trap frequency depends on the offset from the center. This characteristic leads to effects on the dynamic of the atoms in the trap, that are discussed in more detail in Section 4.5.1.

Close to the center, the electric field strength depends linearly on the distance to the minimum and consequently, the force acting on the Rydberg atom does not depend on this offset. A further analysis shows that the field gradients along both transverse directions are approximately equal in the vicinity of the center and a numerical value of about 3.5 V/mm^2 is found. From this it is possible to calculate the acceleration of an atom with a certain offset from the center along with its trap frequency. The acceleration in standard units is given by

$$\frac{a}{m/s^2} = -\frac{3}{2} a_0 e \frac{\nabla F}{V/m^2} \frac{1}{m_H/kg} nk \tag{3.3}$$

which follows from Eq. 3.2 and the conversion to SI units by the factors a_0 and e, listed in table A.1. Using this formula for the hydrogen Rydberg state n = 30 and k = 25, along with the estimated field gradient of 3.5 V/mm^2 and the hydrogen mass $m_H = 1.6737 \times 10^{-27}$ kg yields an acceleration of 2.01×10^7 m/s^2. For such a Rydberg atom with an offset of $d_1 =$

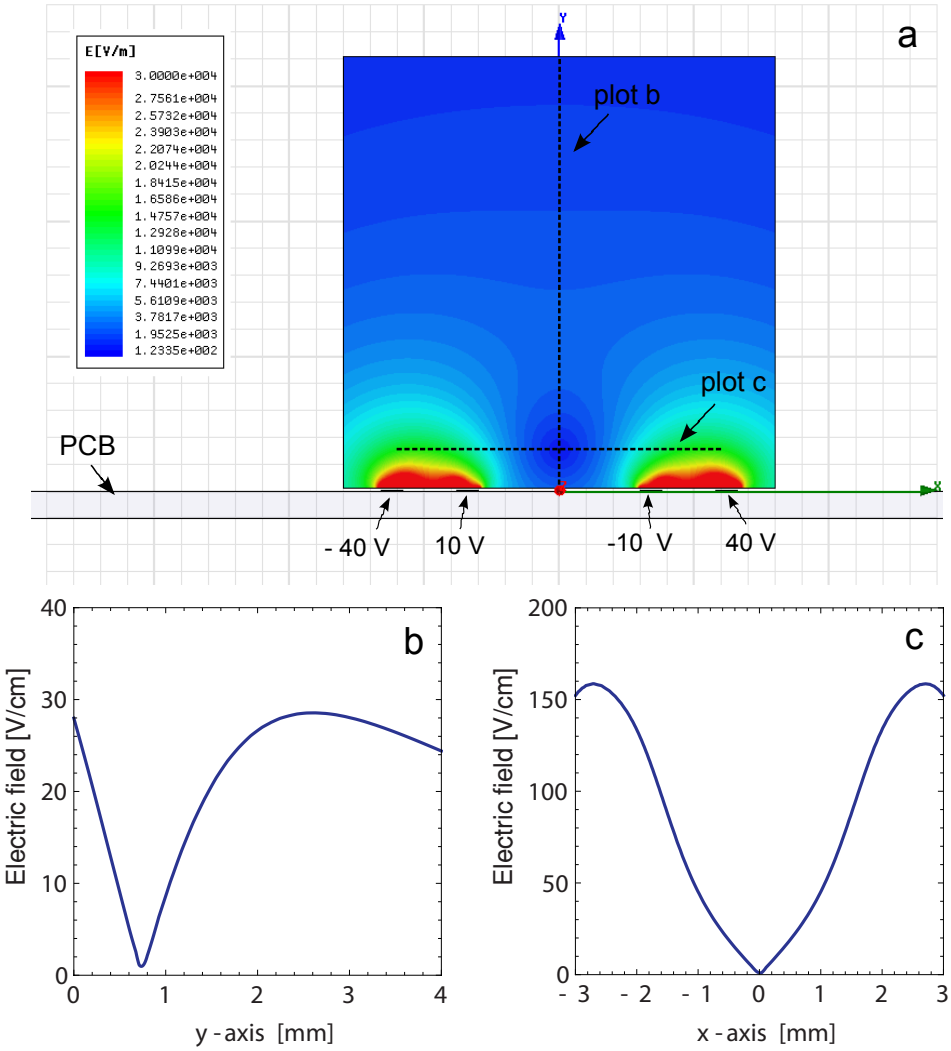

Figure 3.6.: (a) Electric field strength in the plane orthogonal to the surface for the indicated electrode potentials. The dark blue region in the center indicates the local minimum. Plots (b) and (c) show the field strength along the dashed lines in (a) through the minimum. This shows that the transverse trap potential for the Rydberg atoms is not harmonic.

0.5 mm from the axis and zero transverse velocity it therefore takes

$$t_1 = \sqrt{\frac{2\ d_1}{a}} = \sqrt{\frac{2 \cdot 0.5 \times 10^{-3}\ m}{2.01\ m/s^2}} = 7.05\ \mu s \tag{3.4}$$

to reach the center. If the offset was only $d_2 = 0.25$ mm, then the Rydberg atom would need $t_2 = 4.99\ \mu s$ to travel to the guide center, which underlines the anharmonicity of the transverse trap potential. For the later case it takes 20 μs to complete one full oscillation, which corresponds to a trap frequency of $\omega_1 = 50.1 \times 10^3 s^{-1}$, as compared to $\omega_2 = 35 \times 10^3 s^{-1}$ for d_2.

For those numbers to be meaningful, it is essential to relate them to the expected time the Rydberg atoms are exposed to this trap potential. The initial longitudinal velocity of the atoms in the beam is expected to be around 665 m/s. Due to the reduced electric field strength above the chip, the velocity will be higher in the guide as low - field seeking states are considered, but the velocity will be of similar size. From trajectory simulations, which are described in detail in Section 4, a mean velocity of the Rydberg atoms of around 700 - 750 m/s is expected, depending on the applied voltages. For the estimation of the time in the guide a velocity of 725 m/s is used here.

The other unknown parameter in this estimation is the effective length of the guide. In Fig. 3.5 one measures a guide length of 7.4 mm, given as the distance where the four electrodes are parallel. A 3D field simulation of the quadrupole field reveals that at the beginning of the chip the potential minimum is no longer parallel to the surface (see Fig. 3.7), as expected from the idealized two dimensional simulations, but is curved in negative y direction.

An easy way to circumvent this problem is to use time dependent voltages on the electrodes

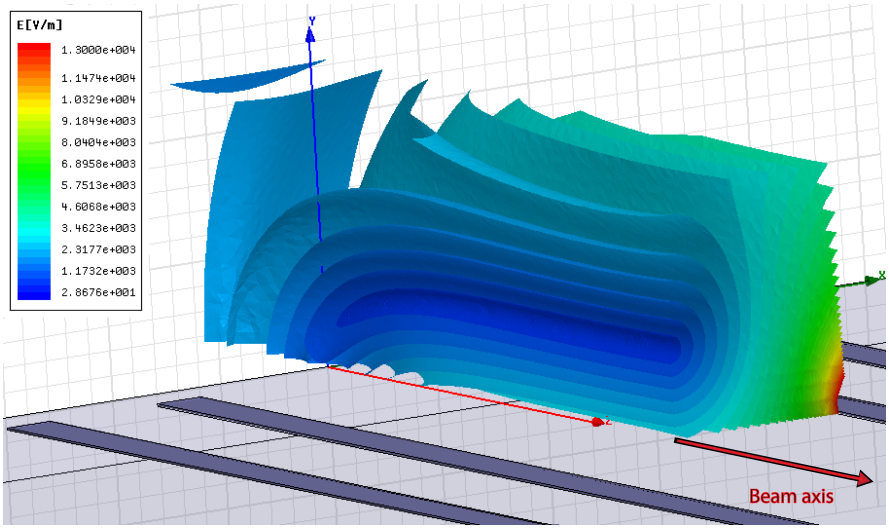

Figure 3.7.: 3D simulation of the electric field of the guide electrodes. In the transverse plane at the center of the guide, the field distribution agrees well with the 2D simulation shown in Fig. 3.6. At the beginning of the PCB, though, the minimum bends towards the PCB surface.

for the guide, such that the voltages indicated in Fig. 3.6 are applied to the electrodes only

if the atoms are within the region where the guide is parallel to the surface. Otherwise the electrodes are set to ground. Due to the small electronic structures it is assumed that the trap potential can be turned 'on' very fast[5].
From the contour plot in Fig. 3.7 and the maximum guide length of 7.4 mm, an effective length of 5 mm is estimated. With an average velocity of 725 m/s this leads to a time of $6.82\mu s$ in the guide, which is relatively short compared to the above calculated oscillation time of around 20 μs.

[5] If one assumes a rise time of 50 ns, which can be considered as an upper limit, then the the Rydberg atoms advance by 36 μm which corresponds to less than one percent of the total length of the guide.

4. Trajectory Simulations of Rydberg atoms

4.1. Introduction

In the planned experiments the interaction between two different physical systems will be investigated, a photon-mediated interaction between atomic and solid state degrees of freedom. Apart from the size of the two systems, the most obvious difference is their mobility. While the individual atoms can freely move in space, the solid state device is fixed. Nevertheless, to make predictions about the effects of the interaction, one needs to know their relative position at any time during the experimental cycle.
As an analytic solution of the equation of motions is unfeasible, numerical methods are used to simulate the trajectories. For a given experimental setup there is a series of steps to be done in order to obtain the trajectories of an ensemble of Rydberg atoms, as schematically shown in Fig. 4.1.

The force acting on a Rydberg atom and therefore the classical trajectory is determined by

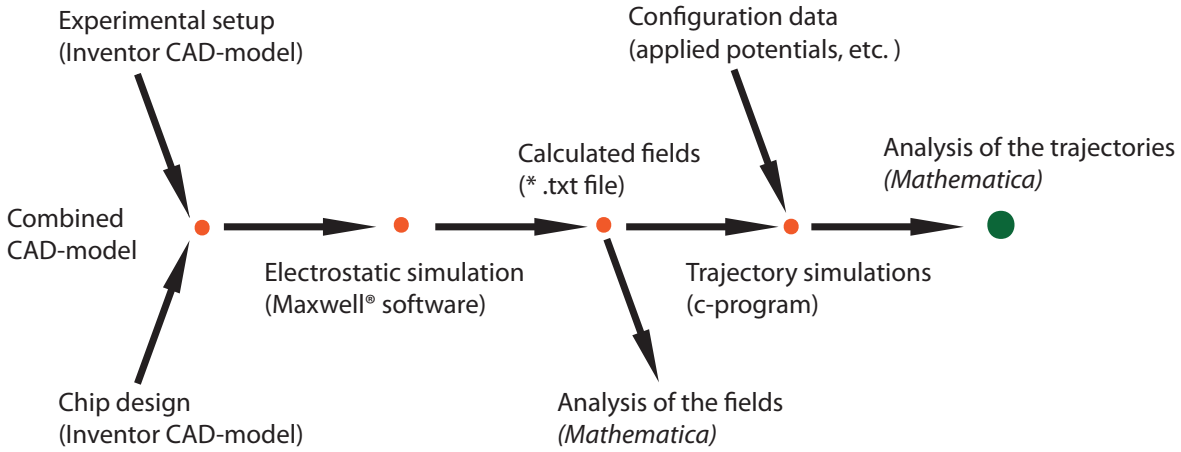

Figure 4.1.: Sequence of operations for the trajectory calculation. The electric field in the model of the experiment is simulated with Maxwell and evaluated on a grid. The field at these points is written to a text file, which is used for the trajectory simulation of the Rydberg atoms.

the applied electric field, as it is described in Section 2.6. To calculate these fields, the first step is to define the exact geometry of all relevant parts, comprising the electrode stack (Fig. 3.1), the PCB-electrodes (Fig. 3.5) and the MCP detector (Fig. 3.3). The assembly of the

different parts is done with the *Autodesk Inventor* CAD program.
In the next step, this CAD model is passed to *Ansoft Maxwell*, a software employing a finite element method (FEM) to solve the electrostatic problem and to calculate the electric fields. For a given potential configuration these fields are then written to a text file which ensures greatest flexibility for further processing. The fields can afterwards be analyzed in detail within *Mathematica*.
Using the field data from the *Maxwell* simulation the trajectories of the Rydberg atoms are subsequently calculated in a C-program. At selected times in the experimental cycle, all relevant parameters, such as position and velocity of each atom in the ensemble, are written to a file. In the post processing these results are visualized in plots of the spatial distribution of the atoms or the evolution of the phase space in time. These simulation are expected to predict the effects that are seen in the experiment, or the other way round, to evaluate and interpret the obtained data [30, 21].

4.2. Simulation of the electric fields

4.2.1. Poisson's equation and the finite element method

The finite element method (FEM) is a powerful numerical method which can be used to solve a wide range of boundary value problems, such as the Poisson equation [43]

$$\nabla^2 \psi = -g \,, \tag{4.1}$$

where g is the source function. For an electrostatic problem g is given by ρ/ϵ_0 , where ρ is the charge density distribution. In most cases it is not possible to solve this partial differential equation analytically, and an approximate numerical solution must suffice.
The simplest method is to discretize space to reduce Eq. 4.1 to a set of linear equations. The solution of these equations yields approximate values of ψ at the discrete grid points. This method is called finite difference method. If irregular geometries or inhomogeneous fields are considered, FEM is advantageous.
The underlying idea of this method is that the solution of the field ψ is patched together from a discrete set of continuous functions rather than just the results obtained at the grid points [44]. The method is probably best explained in two dimensions. The starting point is the requirement that the approximate solution ψ fulfills [43]

$$\iint_R \left[\nabla^2 \psi + g \right] \phi \, dxdy = 0 \,. \tag{4.2}$$

Here $\phi(x, y)$ is a piece - wise continuous weighting function with $\phi|_{Boundary(R)} \equiv 0$, where R is the region where the problem is to be solved. In this method the solution is approximated by a superposition of functions $\phi_{i,j}(x, y)$ which are only nonzero in a finite area around the

grid points (x_i, y_i),

$$\psi(x,y) = \sum_{k,l}^{N} \Psi_{kl}\phi_{kl}(x,y)\,. \tag{4.3}$$

Here, N is the number of all rectangular grid points. The choice of the functions $\phi_{i,j}(x,y)$ is not unique and a possible set is given in Ref. [43]. In the next step, the coefficients Ψ_{kl} are calculated. This is done by using Green's identity for the first term in Eq. 4.2, replacing ψ by the expansion Eq. 4.3 and by inserting $\phi_{i,j}(x,y)$ for the weighting function in Eq. 4.3. One then arrives at [43]

$$\sum_{k,l}^{N} \Psi_{kl} \iint_R \nabla\phi_{ij}(x,y) \cdot \nabla\phi_{kl}(x,y)\; dxdy = g(x_i,y_j) \iint_R \phi_{ij}(x,y)\; dxdy\,. \tag{4.4}$$

Here, the indices i and j run over all N' inner grid points and on the right hand side it was assumed that the source function $g(x,y)$ varies only slowly on the scale of a grid square, such that it can be taken out of the integral. After solving the integrals in the above Equation 4.4 a system of N' coupled linear equation remains to be solved to obtain the coefficients Ψ_{kl}.
So far, a rectangular grid is assumed. This is, however, not a requirement if the basis functions are not explicitly specified. In most applications the base element is not a square, but a triangle defined by three grid points, as they have proven to be most efficient [44]. For the transition from the two to the three dimensional case one adds a further grid point above the surface defined by the triangle in order to realize a tetrahedron. The volume in which the differential equation is to be solved is then covered by these tetrahedrons, but the principle of the calculation remains the same [43] as in the two dimensional case.
The size and the shape of these elements can vary in order to cover the region R with a mesh which fits best the underlying problem. This means, that in areas where the solution varies rapidly, the density of triangles or tetrahedrons is increased, whereas in other regions the density is reduced to save computation resources.
Fig. 4.2 shows the mesh used to calculate the electric field strength of the quadrupole field above the PCB, illustrated in Fig. 3.7. Close to the electrodes the density of the tetrahedrons is increased, while it is lowered towards the edge of the PCB. The mesh of the vacuum is only shown in a selected region above the chip. There the maximal size of the mesh was manually reduced, in order to obtain a smooth solution with a high accuracy.

This method of adjusting the size and shape of the base elements is called adaptive mesh refinement and can be of great importance for certain problems. If one considers the experimental setup shown in Fig. 3.1, it is immediately apparent that the metallic structures on the chip are much smaller in size than the stack electrodes. For an accurate solution it is essential that the mesh above the chip is very fine to account for the fact, that the electric fields vary over small length scales. In the excitation or ionization region, however, the fields will be almost homogeneous, allowing to use a coarser mesh.
It is important to note that if a homogeneous grid over the whole geometry was used instead,

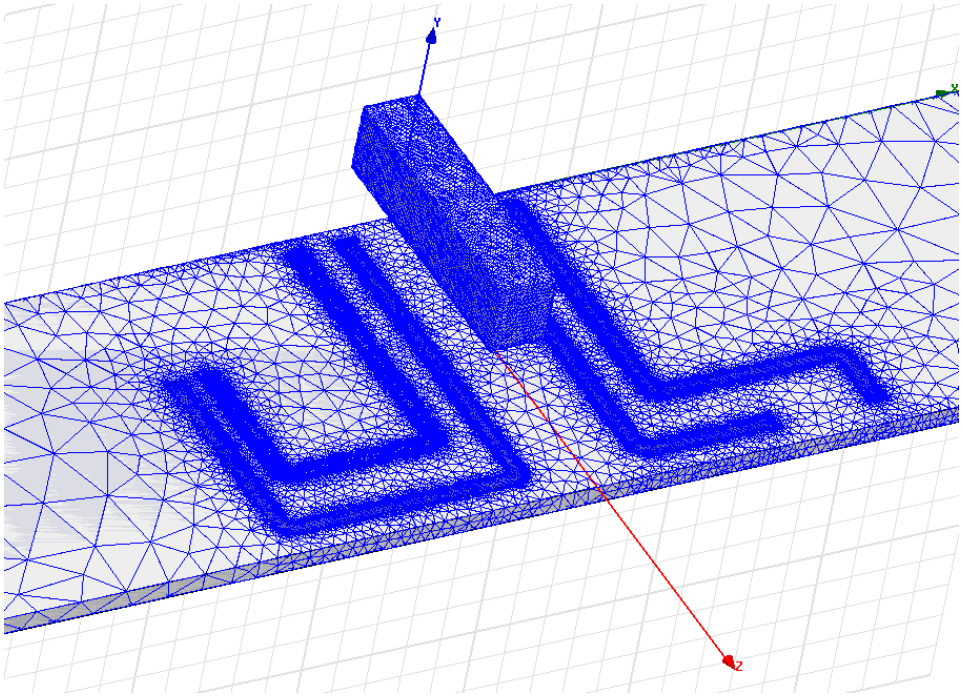

Figure 4.2.: FEM - mesh used to calculate the quadrupole electric field, displayed in Fig. 3.7. Close to the on-chip electrodes the mesh density is increased to account for the rapidly varying electric fields. The box above the PCB shows a selected region of the vacuum, where the size of the tetrahedrons was manually reduced.

which accurately takes the small structure into account, it would be impossible to solve the electrostatic problem on an ordinary computer due to the extensive memory requirement .

4.2.2. Maxwell software

The simulation software used to calculate the electric fields was *Ansoft Maxwell 12.2*. Only some of the key features will be discussed here and this paragraph is not intended to be a guide on how to use this software.

As indicated in the flowchart in Fig. 4.1, the *Inventor* CAD model of the experimental setup can be used in *Maxwell*, which greatly simplifies the whole simulation procedure. There is an internal routine which corrects the CAD model to meet the *Maxwell* standards, such that the program recognizes the individual components of the model. This enables to assign to each part in the setup the correct material and later also a selected potential.

Maxwell uses an automatic adaptive mesh technology [45]. As described in the last section this is in particular important if structures of substantially different size are simulated. In addition it is possible to define regions with a refined mesh, where one can assign the maximal distance between two gird points. Here this is used along the whole beam axis, to ensure that the fields used for the trajectory calculation of the Rydberg atoms are sufficiently smooth and as accurate as necessary.

As soon as the electrostatic problem is defined, i.e. the potentials on each electrode along

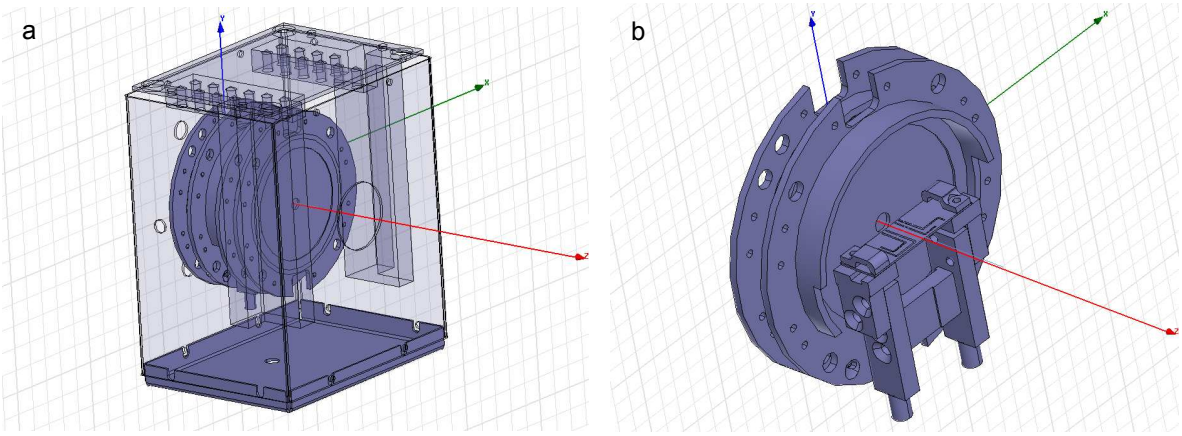

Figure 4.3.: Complete model, apart from the MCP detector, that was used to simulate the electric fields for the subsequent trajectory simulation. (b) First two electrodes and PCB.

with the boundary conditions are set, the electric field is calculated. The solution process is iterative, where in each iteration step the problem is solved for a certain number of tetrahedrons. After each step the electrostatic energy of the approximate solution is calculated and compared with the one of the previous step. If the relative change is very small, this indicates that the solution converged and that a further refinement of the mesh would not yield a substantial improvement [45].
A threshold for this relative change can be set in advance, which is then the stopping criteria for the simulation. The default value for this limit is 1 % but can be reduced if a more precise result is required. This however does not allow to make a quantitative statement about the error of the solution, but is only an indication for the accuracy of the field simulation [45].
Figure 4.3 (a) shows the full model used to calculate the electric fields in *Maxwell*. This includes the electrode stack as well as the innermost shield. The effect of the rest of the experimental setup (Fig. 3.1) on the electric fields along the beam axis within the electrode stack is minimal and not relevant for the trajectories of the Rydberg atoms.

Calculation of the fields by superposition

The electric fields calculated in *Maxwell* are always for a static potential configuration. However, in the experiment the fields are time dependent, as it was discussed in Section 3.4.2. This means that a static potential configuration A changes to another static configuration B. These time dependent fields for the trajectory simulation are calculated with the linear superposition principle in the following way.
If one considers two electrodes, then the electric field strength F in between is proportional to the applied voltage difference. If in addition an external field $\vec{F}_{ext}$ is applied, then the total electric field at each point is given by $\vec{F}_{tot} = \vec{F} + \vec{F}_{ext}$, which is a direct consequence of the linearity of Maxwell's equations in vacuum.
In the experimental setup there are nine electrodes in total where a potential can be applied.

The electric field is then calculated for each electrode individually, which means that one volt is applied to electrode n, while at the same time all the others are pulled to ground. The solution of each field is written to a file, which later enables to calculate the electric field at any point for an arbitrary potential configuration.

4.2.3. Results of the electric field simulations

The results of the electric field simulations can be visualized and analyzed in *Maxwell* directly (Fig. 3.6), but for a detailed study this is not sufficient. For the prediction and interpretation of the trajectories of the Rydberg atoms, it is important and instructive to know the field distribution in the transverse plane to the beam axis. This is in particular relevant above the chip, where the fields of the guide shall be dominant. Most conveniently this analysis is done in an external program, such as *Mathematica*.
The model which is finally used for the simulation in *Maxwell* and the subsequent trajectory calculation is shown in Fig. 4.3. The difference to the model in Section 3.4 is that the PCB with the on - chip electrodes is not studied as an isolated system, but is incorporated in the electrode stack. The applied voltages on the stack electrodes one to four are −97.5 V, −7.5 V, 7.5 V and 97.5 V, which corresponds to the configuration shown in Fig. 3.4 (c). The electrodes on the PCB are set to the alternating potentials of −40 V, 10 V, −10 V and 40 V respectively, which agrees with the values used for the simulations shown in Fig. 3.6 and 3.7. The simulation and subsequent calculation of the electric fields is performed as described in paragraph 4.2.2 and Fig. 4.4 shows the electric field strength in the transverse plane at various positions along the beam axis, measured from the first stack electrode. The y-axis corresponds to the distance from the chip surface, while the x-axis is the offset from the beam axis.
In the vicinity of the center of the guide, one observes that the field strength grows linearly at approximately the same rate in both transverse directions, as shown in Fig. 4.4 (b). This is a characteristic of a quadrupole trap [46] and agrees with the previous results found in Section 3.4. However, the minimum is slightly off the beam axis in Fig. 4.4 (b) and (c). The reason for this is that the arrangement of the electrodes on the PCB is not symmetric, as explained in 3.4.1, but the effects on the fields are more pronounced than expected.
At the beginning of the PCB the field is highly asymmetric as shown in Fig. 4.4 (a). This is not due to the asymmetric geometry of the on-chip electrodes, but due to the short distance to the second stack electrode, which is set to −7.5 V, and the alternating voltages applied to the guide - electrodes on the chip.
Towards the end of the PCB the field minimum is shifted upwards, as shown in Fig. 4.4 (d). At this point, as indicated in Fig. 4.4 (e), only the inner two electrodes remain close to the beam axis. Therefore the field generated by the outer guide electrodes, which close to the chip surface points into the opposite direction of the field between the inner electrodes, is

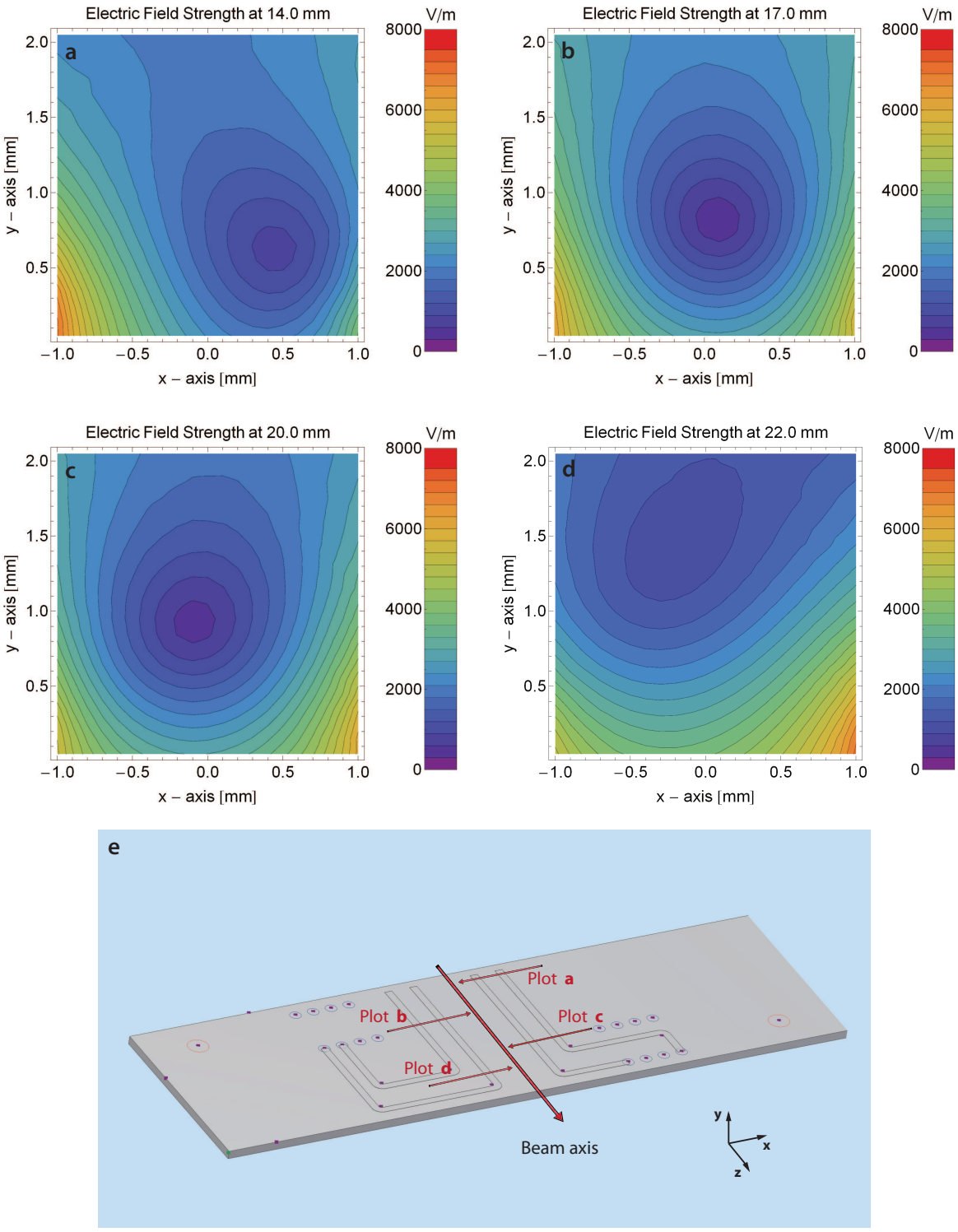

Figure 4.4.: (a)-(d) Quadrupole field in the transverse plane at the positions indicated in (e). The applied voltages on the PCB-electrodes were -40 V, 10 V, -10 V and 40 V and -97.5 V, -7.5 V, 7.5 V and 97.5 V on the stack electrodes. (b) and (c) agree well with the previous 2D simulation, shown in Fig. 3.6, where only the PCB was considered, but at the edges in (a) and (d) the minimum is shifted due to the short distance to the stack electrodes.

missing. It follows that the field strength in this region is increased at low heights.
In Section 3.4 it was suggested to use time dependent potentials on the on-chip electrodes to avoid the effects of the finite length of the guide. The above simulations now underline this need in order to avoid an undesired deflection of the Rydberg atoms from the beam axis at the edges of the quadrupole guide.

4.3. Equations of motion and numerical methods

The classical equations of motion of a particle are determined by its mass and the exerted force on it. Here the particle of interest is the hydrogen atom with a mass of $m_H = 1.6737 \times 10^{-27}$ kg and the force acting on the atom proportional to the field gradient, see Eq. 3.2 and 3.3 [1]. For all spatial directions x_i one finds the differential equations

$$\ddot{x_i} = -\frac{3}{2} e a_0 \frac{1}{m_H} \frac{\partial F(\vec{r}, t)}{\partial x_i} nk, \tag{4.5}$$

which governs the motion of the Rydberg atoms in the electric field. To calculate the trajectories of these atoms, this equation needs to be solved numerically.

4.3.1. Numerical methods to solve an ordinary differential equations

An ordinary differential equation (ODE) of first order can be written as [44]

$$\frac{dy}{dt} = f(y, t) \quad \text{with} \quad y(t_0) = y_0, \tag{4.6}$$

which has exactly one solution if the initial value y_0 is given and the function f is continuous [47]. The solution then satisfies the relation

$$y(t) - y_0 = \int_{t_0}^{t} f(\tau, y(\tau))\, d\tau \,. \tag{4.7}$$

However, in most cases it is not possible to find a closed form of the solution, such that numerical methods need to be employed. In these methods the time is discretized and one advances in steps of Δt. A starting point for these methods is the Taylor expansion of the function at the time t,

$$y(t + \Delta t) = y(t) + \Delta t \frac{dy}{dt} + \frac{(\Delta t)^2}{2} \frac{d^2 y}{dt^2} + \dots \,. \tag{4.8}$$

If only terms up to linear order are considered, one arrives at the Euler method

[1] Another force acting on the particle is of course the gravity which, in the context of this experiment, can safely be neglected. If one assumes an upper limit of 200μs for duration of the experimental cycle, then the gravity would lead to a vertical shift of the atoms of 200 nm, which is below the spatial resolution of an MCP.

$$y_n = y_{n-1} + \Delta t f\left(y_n, t_n\right), \tag{4.9}$$

where $t_n = t_{n-1} + \Delta t$ and $y_n = y\left(t_n\right)$. This is the simplest method to to solve an OED, but in each step an error proportional to $(\Delta t)^2$ is accumulated. As there are a total of $n = \frac{T}{\Delta t}$ steps, the error over the whole time interval T is proportional to Δt.
If in the Taylor expansion in Eq. 4.8 terms up to second order are considered, a slightly refined method can be formulated. The idea is that the slope $\frac{dy}{dt}$ is calculated in the middle of the interval Δt, rather than at the beginning as it is done in the Euler method. This will lead to a correction which takes the curvature of the function $f\left(y, t\right)$ within the interval Δt into account.
In this method, which is called 2^{nd} order Runge Kutta, one starts from time t with an Euler step of size $\Delta t/2$ to calculate $y\left(t + \Delta t/2\right)$. At this point the slope $\frac{dy}{dt} = f\left(y, t\right)$ is calculated which is used to advance a full time step from the time t. The iteration step is therefore given by

$$y\left(t + \Delta t\right) = y\left(t\right) + \Delta t\ f\left[y\left(t + \frac{\Delta t}{2}\right), t + \frac{\Delta t}{2}\right] \tag{4.10}$$

The error in each step is proportional to $(\Delta t)^3$ which is an improvement compared to the Euler method. For the explicit numerical calculation this means that in order to achieve the same accuracy as with the Euler method, the time steps Δt can be chosen to be larger, which can considerably increase the efficiency of the calculation.
There are much more advanced methods to numerically solve ODEs, in particular the Runge Kutta methods of higher order [47]. These methods can lead to an improved efficiency by allowing larger time steps Δt or an increased accuracy for fixed Δt. At the same time the complexity and the computation time for each step increases, such that a higher order method is not automatically the better choice
For the trajectory simulations of the Rydberg atoms it was decided to use the 2^{nd} order Runge Kutta. This was motivated by the observation, that with this technique the calculated trajectory for a single atom is only slightly different to the one calculated with the Euler method. This allows to draw the conclusion, that for the same Δt a higher order method would not yield a substantial difference. On the other hand, Δt can not be increased by much even if a more advanced numerical method was used, as the slew rates of the time dependent fields need to be considered. From the point of efficiency and accuracy 2^{nd} order Runge Kutta is the optimal choice.

Second order differential equation

A second order ODE like $\ddot{x} = f\left(x\right)$ in Eq. 4.5 can be transformed into two coupled OEDs of first order, as illustrated by [44]

$$\ddot{x} = f(x) \quad \Rightarrow \quad \begin{cases} \dot{x} = v_x \\ \dot{v}_x = f(x). \end{cases} \tag{4.11}$$

In the Runge Kutta method the coupling of the equation needs to be taken into account and in each time step Δt, the following four operations are executed for each spatial direction x_i in this order:

1. $x_i[t + 0.5\,\Delta t] = x_i(t) + 0.5\,\Delta t\; v_i(t)$
2. $v_i[t + 0.5\,\Delta t] = v_i(t) + 0.5\,\Delta t\; f[x_i(t), t]$
3. $x_i[t + \Delta t] = x(t) + \Delta t\; v_i[t + 0.5\,\Delta t]$
4. $v_i[t + \Delta t] = v_i(t) + \Delta t\; f[x_i(t + 0.5\,\Delta t), t + 0.5\Delta t]$

In the trajectory calculation for the Rydberg atoms, this method is implemented with a slight modification. In the fourth step, the explicit time dependence of $f(x, t)$ is neglected. This is justified by the fact that the slew rates of the potentials on the electrodes are either slow enough, such that in each sufficiently short time interval static fields can be assumed or so rapid, that the the change of the potentials can be considered to be instantaneous. Furthermore, the computational cost would be too high and the including of this time dependence would not be warrantable.

4.4. Trajectory simulation in a C program

The aim of this section is to describe the principle and the realization of the trajectory simulation in the C - program. Based on the equation of motion 4.5 and the numerical methods derived above, the task of the C - program is to calculate the trajectories of the Rydberg atoms and to return them in a way that allows a convenient analysis and interpretation of the results.
Similar to the flowchart in Fig. 4.1 in the beginning of this chapter showing the whole simulation procedure, Fig. 4.5 only illustrates the different operations executed by the C - program. It can therefore be viewed as a detailed description of the point 'Trajectory simulations' in the initial flowchart.

4.4.1. Configuration data

The initially read configuration file sets certain parameters to their desired values. This are in particular parameters, which can easily be changed in the experiment such as the applied potentials to the different electrodes and their time dependence. For the guide electrodes one can define at what time they should be set to the desired voltage and at which time to turn them off again. Also it is not yet clear which quantum numbers n and k will be used, and in

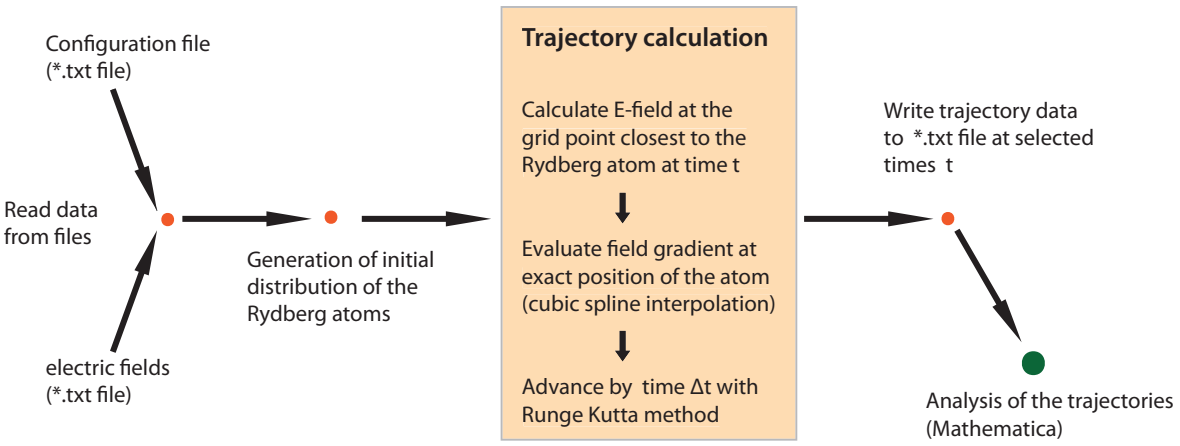

Figure 4.5.: Flowchart of the trajectory simulation program. In the first step, the program imports the electric field data and the parameters for the simulation from the configuration file. Then, the equation of motion is solved for each time interval. In the last step, the data of the trajectories of the Rydberg atoms is written to a text file.

the experiment one is quite flexible within a range of about $n = 20$ to $n = 35$ [33]. Therefore it is desired to have the ability to easily change these values in advance of a simulation.
For the imaging and the internal state spectroscopy described in Section 3.3, the applied voltages in the field ionization region are of great importance. The relevant parameters are the height of the ionization pulse and its duration. This can currently be done for a perfect square pulse, which is to be defined in the configuration file.
In principle all those parameters could be set directly in the C - code, but the configuration file is used to avoid the necessity to recompile the code for each change in a parameter.

4.4.2. Import the electric fields calculated with Maxwell

A crucial and at the same time rather delicate task is to read in the electric fields calculated with *Maxwell*. Crucial, because the trajectory simulation fundamentally depends on these fields as they determine the force exerted onto the atom. And the difficulty of this process is mainly given by the size of the files and their exact structure.
The field calculated in *Maxwell* is evaluated at discrete grid points and written to a text file. The size of this file is given by the size of the grid, and the spacing between these points. The currently considered points are along the beam axis, bound in transverse direction by the size of the openings in the electrodes, illustrated in Fig. 4.3. The grid spacing is chosen to be 0.1 mm, which seems reasonable considering the length scales over which the field strength changes, shown in Fig. 3.6 and 4.4. This results in a size of the text file of around 250 MB. As it is required to read in this field data for each individual electrode, as described above in Section 4.2.2, this gives a total of around 2 GB of memory that is required during the

simulation.
For the hardware of a modern computer this is hardly a problem, but it indicates that the resolution cannot be refined by much. If the resolution was enhanced by a factor of two in each spatial direction, this would increase the required memory by a factor of 8, which exceeds the available memory of commercially available computers.
In the program the whole field data is internally stored in a single array or variable. Due to the large amount of memory, it is required to manually allocate enough memory to this variable, which is known as dynamic memory allocation [48]. Another subtlety is the exact structure of the text file created by *Maxwell*. The data is read in as a string and subsequently converted to a floating point number.
For the current version it takes less than 20 seconds to read in the 2 GB of data, which corresponds 90 % of the maximum transfer speed of data from the installed hard drive[2]. This indicates that the implemented function to import the data is most efficient.

4.4.3. Initial distribution of the Rydberg atoms in the excitation region

Before the trajectories of the Rydberg atoms can be calculated, the initial positions within the experimental setup need to be set, as described in Chapter 3. The excitation of the atoms by the laser is not explicitly simulated, but an initial distribution of the Rydberg atoms with quantum numbers n and k is assumed. The parameters chosen for this distribution were obtained in a previous experiment (Reference [21]) and adapted for the specific characteristic of the current experimental setup. In the first experiments these parameters should be determined in order to be used in further simulations. The initial spatial distribution is mainly given by the width and direction of the laser beam which leads to a cigar-shaped distribution perpendicular to the beam direction, as shown in Fig. 4.6. The velocity distribution in longitudinal and transverse directions can be inferred from Time of Flight (TOF) spectra and the spatial distribution at the MCP detector, respectively [35]. The velocity distribution in each spatial direction is given by the normal distribution

$$f_v\left(v_i\right) = \sqrt{\frac{m}{2\pi k_B T}} \exp\left[-\frac{m v_i^2}{2 k_B T}\right]. \tag{4.12}$$

where m is the mass of the hydrogen atom and T the temperature associated with the relative kinetic energy, as defined in Section 3.1. In the initial distribution the temperature in x - direction (which is along the laser beam) will be higher than in the y - direction (perpendicular to the beam axis and the laser beam). The reason for this is the following. Due to the finite width of the laser beam, it will only excite atoms which are sufficiently close to the beam. As the initial cloud of hydrogen atoms in the ground state propagate from the skimmer to the excitation region, the fast or 'hot' atoms moved further in transverse direction than the slow or 'cold' atoms. This has the effect that 'hot' atoms are too far away from the laser beam to

[2]The maximum data transfer rate is 125 MB/s , which is given in the data sheet of the installed ST3320418AS hard drive.

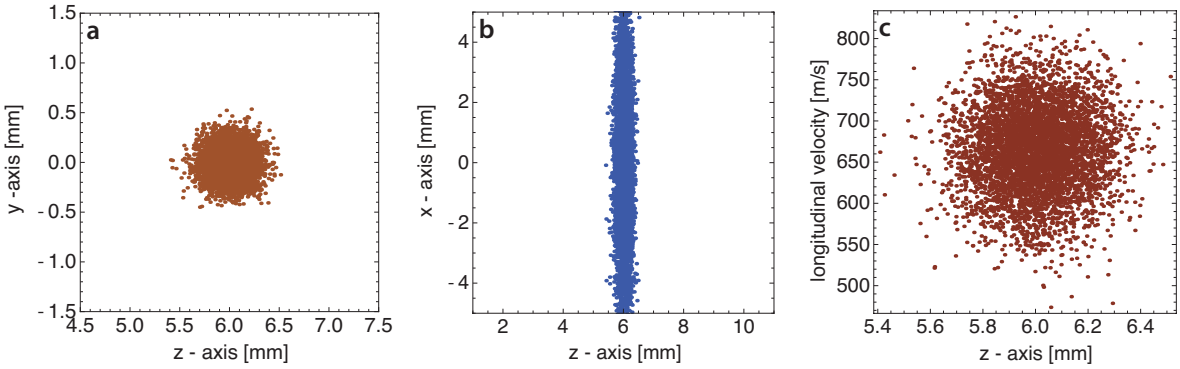

Figure 4.6.: (a) Initial spatial distribution of Rydberg atoms in the x-y plane. The diameter of the cloud corresponds approximately to the width of the laser beam. (b) 'Top-view' of the atom cloud in the z-x plane. (c) Phase space in the z-direction. The mean longitudinal velocity is 665 m/s.

be efficiently excited. In the x - direction however, all atoms are excited, which then leads to this difference of the two transverse velocities and the initial spatial distribution of Rydberg atoms, as illustrated in Fig. 4.6.

4.4.4. Calculation of the electric field at the grid points within the C - program

As mentioned previously, it is desired to apply time-dependent potentials. This requires to read in all the electric fields generated by the individual potential of a single electrode and to calculate the resulting electric field at each point by superposition, as described in Section 4.2.2.

The field strength at a specific grid point is calculated in the following way. The field $\vec{F}_i$ generated by a single excitation of electrode i is scaled with the desired voltage at time t on electrode i. Then the sum

$$\vec{F}_{tot} = \sum_{i=1}^{N} \vec{F}_i \tag{4.13}$$

is taken, where N corresponds to the number of electrodes. As $\vec{F}_{tot}$ is the electric field vector containing the fields of all spatial directions, its length then corresponds to the field strength at the respective grid point.

4.4.5. Calculation of the field gradient and the Runge Kutta step

To calculate the force exerted onto the Rydberg atom, the gradient of the electric field strength needs to be calculated, as stated in Eq. 3.2.

In the first step, the Rydberg atom needs to be positioned in the grid, hence the closest grid points are determined. With the knowledge of the electric field strength at the adjacent points, the gradient can then be derived. Previous trajectory simulation programs have indicated, that this calculation needs to be done carefully. In particular it was observed, that it is not

sufficient to linearly interpolate the field strength between two point to obtain the partial derivative.
To calculate the partial derivative along the spatial direction x_i it was decided to employ a cubic spline interpolation between the four closest grid points along x_i and to take the derivative of this function at the position of the Rydberg atom.
To implement this method efficiently, the free[3] GNU scientific library (GSL) is used, which is extensively described in Ref. [49]. This library includes many commonly used numerical methods, as well as different pseudo random number generators.
The interpolation method employed here assumes natural boundary conditions, which means that the second derivative at the boundary point is taken to be zero [47]. The same library includes as well the function to evaluate the derivative at any point along x_i.
If the gradient of the field strength is known, the force acting on the Rydberg atom can be calculated and the Runge Kutta iteration step can be executed as described in the Section 4.3.1.

4.4.6. Output of the simulation data

As indicated in the flowchart 4.5, the results of the simulation are written to a text file to enable a convenient post analysis. The parameters of interest of the ensemble of Rydberg atoms are mainly the spatial distribution, as well as the phase space density distribution. The latter becomes particularly relevant if the trapping of the atoms is investigated, as described nicely in [29]. For this reason, the position and the velocity vector of each particle is written to a file at preselected times during the experimental cycle. At present, this data is recorded every 100 ns, which roughly corresponds to 70 μm travelled in longitudinal direction and therefore allows to observe the evolution to the atom cloud in detail.

4.4.7. Speed up of the program

In the development of the simulation program, the execution speed did not have immediate priority, but was optimized at some relevant points. In this context it is important to know the sequences in the code, which are computationally most expensive. In the current version, this is in particular the calculation of the electric field at the desired grid points with the subsequent spline interpolation. In principle this calculation needs to be done for each atom at every time step.
The longitudinal velocity is relatively low compared to the grid spacing, which implies that there are several time steps between two adjacent grid points. By temporally storing the fields calculated at time step n one can reuse the calculated fields along with the interpolation function in time step $n+1$, if the particle is still within the same grid points. With this method it is possible to substantially improve the efficiency of the program, without affecting

[3] To be precise, 'free' in the context of the GNU General Public License

the accuracy in any way. The required time to simulate a large ensemble of atoms could be reduced by a factor of around 5.
The simulations presented in the next sections were performed with ensemble sizes of about 5000 Rydberg atoms. If better statistics is required, however, samples of up to 10^6 can be considered. In the first case it takes around 2 minutes, in the latter 7 - 8 hours to run the simulation.

4.4.8. Trajectory calculation of the ionized atoms

As described in Section 3.3, the Rydberg atoms are ionized at a specific point. Due to the large ionization fields and the low hydrogen mass, the atoms are accelerated to high velocities towards the MCP detector. In order to predict the spatial distribution of the atom cloud there, the simulation was extended, such that the trajectories of the ions can be calculated. The equations of motion at this stage are given by

$$\ddot{x}_i \left[m/s^2\right] = \frac{F_i \left[V/m\right] \; q \left[C\right]}{m_H \left[kg\right]}, \tag{4.14}$$

where the F_i is the electric field along the spatial direction x_i and q the charge and m_H the mass of the ionized hydrogen atom.
The component F_i of the electric field vector is again calculated by cubic spline interpolation, but the trajectory is calculated with the Euler instead of the Runge Kutta method, since the electric field between the last electrode and the MCP is expected to be sufficiently homogeneous.

4.5. Evaluation of the results of the simulation

After the simulation is performed there are two important points which need to be considered. First, the results have to be visualized in an appropriate way to allow for further interpretations and to relate them to the experimental outcomes. Second, and even more important, is to actually test the simulation, hence to check if the trajectories are calculated correctly.

4.5.1. Testing of the simulation

The testing of the trajectory simulation was done by comparing the predictions of the calculation with results obtained in a previous experiment. This experiment is described in detail in Ref. [21] and therefore only a short description with the most important parameters is given here. The hydrogen Rydberg atoms with $n = 30$ and $k = 25$ were first decelerated by time dependent fields and then loaded into a 2D or a 3D electrostatic trap. The arrangements

of the electrodes is schematically illustrated in Fig. 4.8 (a).
Electrodes 1 - 4 are used to decelerate the Rydberg atoms in longitudinal direction and to later confine them in the z - and y - direction. This then generates a 2D trap and electrodes 5 and 6 can be used confine the atoms as well in the x dimension, leading to a 3D trap. In Fig. 4.8 the z - axis corresponds to the beam - axis of the atoms.
By default, + 20 V (-20 V) are applied to electrodes 1 and 4 (electrodes 2 and 3), which corresponds to a quadrupole configuration with the field strength minimum framed by the electrodes 1 - 4. For the deceleration a large voltage pulse of ±1265 V is applied to electrodes 3 and 4 to generate a highly inhomogeneous electric field with a large positive gradient along the beam - axis [30]. For the low - field seeking Stark states used in the experiment, this leads to the desired deceleration, as described by Eq. 2.34. If an appropriate pulse form is chosen, the atoms are stopped right at the center of the quadrupole field minimum.
The trajectory simulation of the Rydberg atoms for this experimental setup are conducted with the parameters given in [21], with the exception that electrodes 5 and 6 are ignored. This, however, does not affect the deceleration process and the subsequent 2D trapping.
The simulation was done with initially 5000 Rydberg atoms and the obtained results are illustrated in Fig. 4.7 by the spatial distribution in the zy - plane and by the phase space in Fig. 4.8 (b).
The spatial distribution in Fig. 4.7 shows the projection of the atom cloud onto the zy - plane. Therefore, each dot corresponds to the y- and z- coordinate of an atom. This plot is given at different times, measured from the excitation time of the Rydberg state, to illustrate the evolution, deceleration and the longitudinal trapping of the atom cloud. Fig. 4.7 (a) is taken at 6 μs, when the atoms approach the end of electrode 1 and 2 at 13 mm, but before the deceleration pulse is applied. After the deceleration, the dynamic of the atoms in the 2D trap which is located at approximately 14.5 mm is illustrated in Fig. 4.7 (b) to (c), indicating an oscillation of the atoms in the longitudinal direction. At later times, a more homogeneous spatial distribution of the atoms in the 2D trap is observed, such that the oscillation of the cloud is less pronounced. This effect can be better understood by the analysis of the phase space.

The phase space distribution in in the z dimension, corresponding to a plot of the longitudinal velocity v_z vs. the z coordinate of the Rydberg atoms in the cloud, is shown in Fig. 4.8 (b). At 0 μs the initial velocity spread in v_z is indicated, which approximately follows a Gaussian distribution [37]. The tilting of the distribution at 4 μs simply illustrates the fact, that the fast particles travel further than the slow ones in this time interval.
At 8 μs one can see the effect of the deceleration. The atoms which are further along the beam axis are first slowed down, such that all atoms have roughly the same velocity at a certain point. This then corresponds to the illustrated horizontally orientated density distribution in the phase space.
The last plotted distribution shows the phase space at 88 μs, when the atoms were trapped for some time. One can nicely observe a spiraling in the phase space, which originates in the

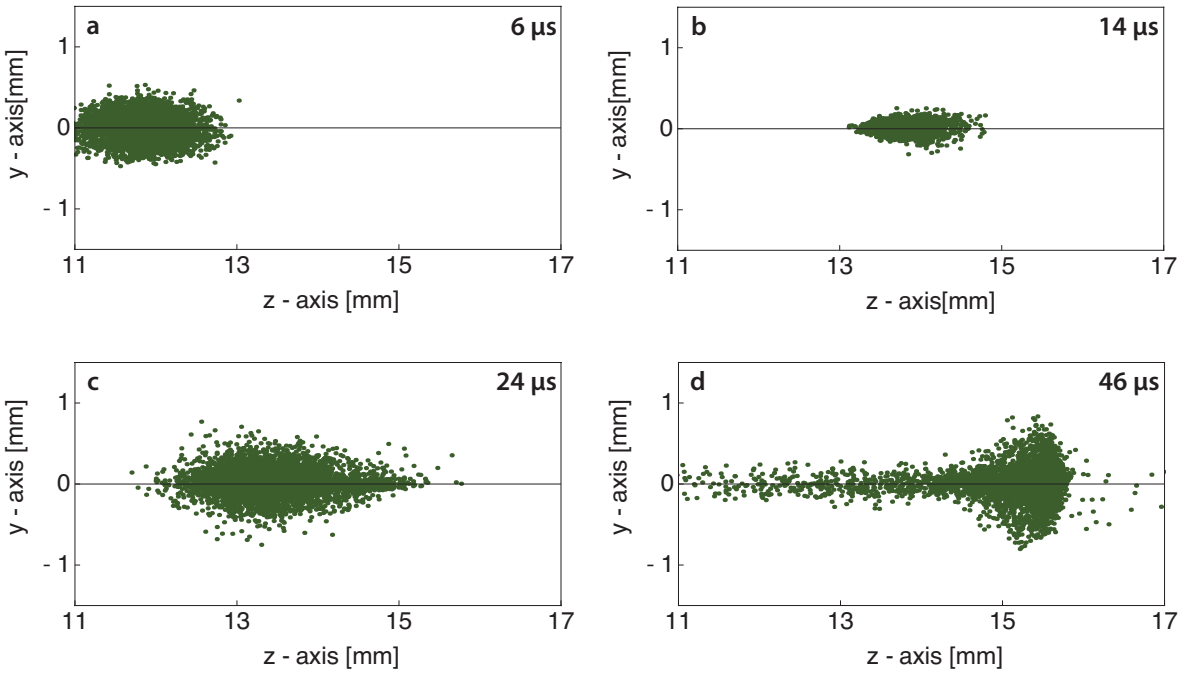

Figure 4.7.: (a) - (c) Spatial distribution of the atom cloud in the z-y plane at different times. The minimum of the quadrupole trap is at approximately z = 14.5 mm. Plot (a) displays the distribution right before and (b) after the deceleration. Figures (c) and (d) show the distribution after different trapping times.

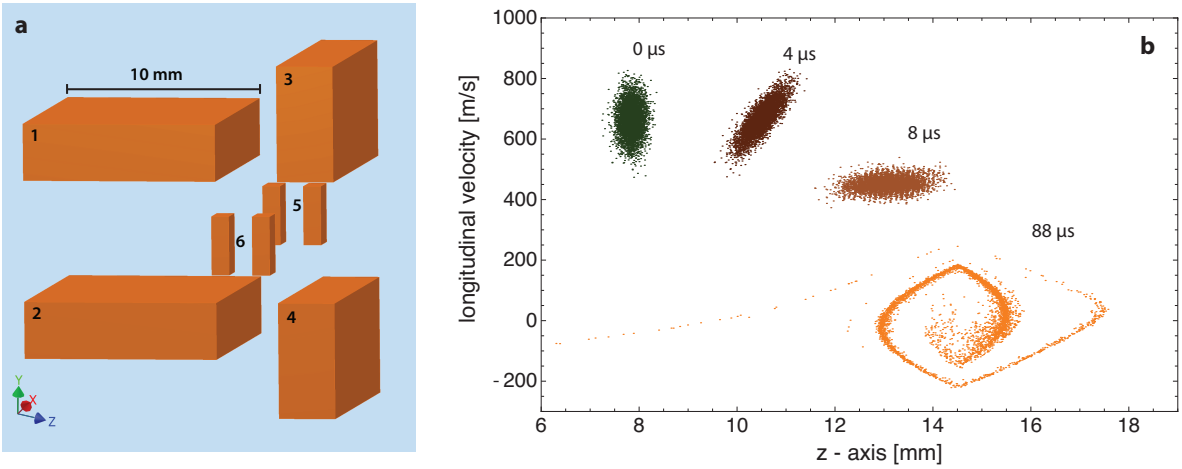

Figure 4.8.: (a) Schematic assembly of the electrodes. Electrode one is 10 cm long. (b) Phase space in the z-direction at different times after the excitation. The tilting and elongation of the phase space after 4 μs corresponds to the normal evolution of the phase space if no force is exerted onto the atoms. After 8 μ the cloud is already slightly decelerated. The spiraling after 88 μ is due to the anharmonic trap potential.

anharmonicity of the trapping potential. The atoms therefore do not rotate with the same frequency in the phase space, as it would be the case for a harmonic trap [29].
The obtained results of the simulation predict the deceleration of the Rydberg atoms and the subsequent 2D trapping, which agrees with the results obtained in the experiment and in previous simulations [21]. This is a strong indication that the developed simulation program correctly calculates the trajectories of the Rydberg atoms and that there are no major errors.

4.6. Review of the trajectory simulation

The simulation of the Rydberg trajectories is important both for the design and the evaluation of the experiment. First, because one expects the simulation to predict the effects of the experiment, which are directly related to the trajectories. Based on these results the experimental setup can be optimized. Second, in order to interpret the obtained results in the experiment, it will be helpful to know the trajectories of the Rydberg atom.
The electric fields which are required for the simulation are calculated with a commercially available finite element program. In a C program the equation of motion is solved numerically and the obtained positions of the atoms are stored at certain times which then allows the analysis of the trajectories.
The C-program was tested by comparing the prediction of the simulation with results from previous experiments. The experimentally observed effects could be reproduced by this simulation, indicating that the calculations are performed correctly.

5. Results of the trajectory simulation

In this chapter, the developed trajectory simulation program for the Rydberg atoms is applied for the experimental setup illustrated in Fig. 3.1, combined with the on-chip quadrupole guide discussed in Section 3.4. The complete model used for the simulation is shown in Fig. 4.3.
The results of the trajectory simulations for different potential configurations of the on-chip electrodes are presented and discussed. Due to the early stage of the experiment it was not possible to compare the simulations with real measurements within this thesis. The obtained results, however, allow to estimate the range of applications of the quadrupole guide and consequently as well its limits.

5.1. Parameters used for the simulation

Quantum numbers of the Rydberg atoms

For all simulations in this chapter the quantum numbers are $n = 30$ and $k = 25$ respectively, corresponding to a low-field seeking state. In the experiment though, it will be possible to excite any state in the range of around $n = 20$ to $n = 35$ [33].
For the selection of the quantum state used in the experiment, its excitation, but as well its detection has to be considered. This is closely related to the required field to ionize the Rydberg atoms, given by Eq. 2.30. For $n = 30$ this field is approximately 1.4×10^3V/cm, where it is 3.0×10^3V/cm for $n = 25$. This then determines the required voltage applied to electrode 3, labeled in Fig. 3.1, to field ionize the atoms.

Applied Voltages

In the simulations the default potentials on electrode 1 to 4 are -97.5V, -7.5V, 7.5V and 97.5V, as indicated in Fig. 3.4 (c). They do not need to be static, but can be time dependent for the ionization.
In the simulation, the MCP is approximated by a cylindrical electrode with a diameter of 15 cm[1] and an applied voltage of -3000 V. The position of the MCP is indicated in Fig. 3.1.
The potentials applied on the on-chip electrodes can be chosen to confine the atoms above

[1] The actual diameter of the MCP is approximately 4 cm, but to avoid inhomogeneous electric fields, the MCP is embedded in an a larger electrode on the same potential

the chip in transverse direction, and depending on the applied voltages, different effects are observed. These potentials are not static, but only 'switched on' when the atoms are right above the chip, as discussed in Sections 3.4.2 and 4.2.3.
The times to apply these potentials are determined by simulating the trajectory of a single particle with the average value for the initial position and velocity of the atom cloud. 12.9 μs (19.7 μs) after the excitation this particle is at 15 mm (20 mm), and the guide is then turned on (off). To turn 'on' and 'off' the trap means that a certain voltage configuration is applied to the electrodes or that the electrodes are pulled to ground, respectively. These positions are chosen such that the Rydberg atoms are only exposed to the quadrupole guide when the potential minimum is aligned parallel to the chip surface, see Fig. 3.7 and 4.4.
In the same way, the ionization time was determined to be 35.3 μs. When the atoms reach the center of the ionization region in Fig. 3.1, a large voltage pulse is applied on electrode 3, see paragraph 5.1. For Rydberg atoms with $n = 30$ and $k = 25$ the applied voltage was 1.5 kV for a duration of 100 ns, yielding a field of around 1.6 kV/cm, slightly above the ionization limit.

Characterization of the atom cloud of excited hydrogen atoms

The parameters for the atom cloud right after the ionization are chosen in agreement with the values given in reference [21]. The initial cloud of excited atoms has a mean longitudinal velocity of 665 m/s. The relative kinetic energy can be expressed as a temperature and is given by $E/k_B = 300$ mK. In the transverse plane the mean kinetic energy in y- and x-direction is given by $E/k_B = 5$ mK and $E/k_B = 75$ mK, respectively. The different values in transverse direction are due to the finite width of the excitation laser (Section 4.4.3).
The laser excites the atoms efficiently only if they are sufficiently close to the laser beam, which determines the initial spatial distribution. In the z-y plane this follows a Gaussian distribution in radial direction with a standard deviation of 0.5 mm, as it is illustrated in Fig. 4.6. In the transverse plane the atoms are initially distributed along the laser beam axis. However, as the atoms proceed along the z-axis, this spread is limited by the width of the hole in the second electrode with a diameter of 5 mm.

5.2. Focusing the atoms

The purpose of the on-chip guide presented in this thesis is to study the effect of the quadrupole field on the trajectories of the Rydberg atoms. The obtained results will carefully be analyzed in order to optimize the geometry and the properties of the guide. In the future this will allow to confine the atoms above the PCB in the transverse direction and to guide the atoms at a short distance across a microwave transmission line.
A force is exerted onto the Rydberg atoms in the quadrupole guide to focus the atom cloud

in the ionization region, as schematically illustrated in Fig. 5.1. This means that the transverse extension is lowest when the atoms are ionized and subsequently accelerated towards the MCP, where the spatial distribution is determined. The experimental realization of this scheme is important to demonstrate the feasibility of the subsequent experiments.

The potentials that need to be applied on the on-chip electrodes to achieve focusing, are

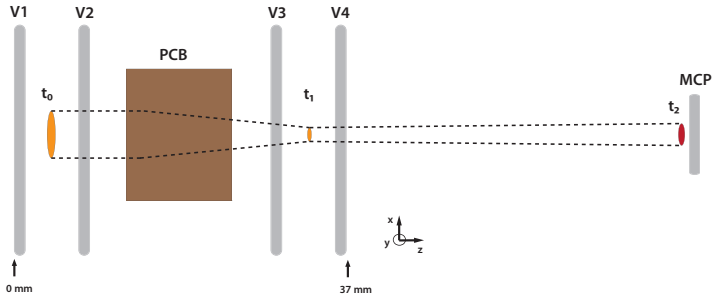

Figure 5.1.: Focusing of the atoms in the ionization region between electrodes V3 and V4. The initial atom cloud at t_0 propagates along the z - axis. Above the PCB the atoms are exposed to the quadrupole field which accelerates the atoms towards the center of the cloud, leading to a focusing in the ionization region between electrode V3 and V4 at time t_1. At time t_2 the spatial distribution of the ionized atoms is recorded with the MCP detector.

determined by scaling the values of the potentials in the previous Section 3.4. Different trajectory simulations are performed and the scaling factor is chosen to minimize the standard deviation in the transverse positions of the atoms in the ionization region. The optimal voltages on the guide electrodes 1 to 4 are found to be -10.6 V, 2.65 V, -2.65 V and 10.6 V, respectively.

Initial distribution of the Rydberg atoms

The initial distribution of the Rydberg atoms in the excitation region is cigar-shaped along the beam of the excitation laser. This is illustrated in Fig. 5.2 (a) and (b), showing the spatial distribution in the x-y and the z-x plane, respectively. In this simulation, the initial spatial distribution is shifted by 0.5 mm in positive y-direction, compared to the one discussed in Section 4.4.3, such that the majority of the Rydberg atoms are at the height of the quadrupole guide, shown in Fig. 3.7. In the experiment, the different lasers are fixed, such that the position of the excited Rydberg atoms cannot be changed. However, to achieve the same effect of adjusting the spacing between the chip and the atoms, it is possible to vary the vertical position of the PCB.

Due to the elongated shape of the atom cloud along the x - axis, the effects of the focusing will be most pronounced in this spatial direction. For the understanding of the evolution of the spatial distribution, it is instructive to monitor the distribution in the phase space in the x-direction, shown in Fig. 5.2 (c). The tilting originates from the propagation of the atoms from the pulsed valve to the ionization region and the relative kinetic energy, see Fig. 3.1. Atoms with negative velocity v_x after the valve will have a negative x - coordinate in

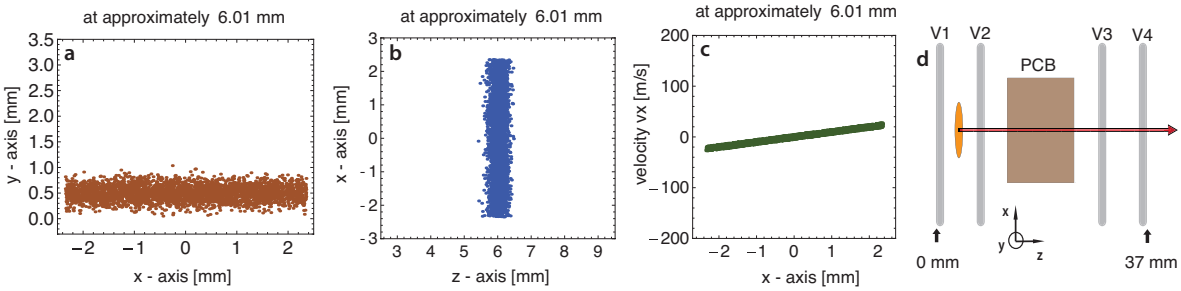

Figure 5.2.: (a) and (b) Initial spatial distribution of the Rydberg atoms in the x-y and z-x plane. The sharp edges of the distribution are a result of the simulation program. Atoms with a radial distance to the beam axis larger than the radius of the holes in the electrodes are removed from the simulation. (c) Phase space in x direction. The velocity v_x vs. the offset form the z-axis is plotted for each atom. (d) Position of the atom cloud (orange ellipse) with respect to the four stack electrodes V1 to V4. The red arrow indicates the propagation direction.

the ionization region. The initial position of the atom cloud with respect to the four stack electrodes is indicated in Fig. 5.2.

After the quadrupole field

After the excitation region, the atoms pass through the opening in the second stack electrode V2 and proceed towards the PCB. After 12.9 μs, when the atoms are above the chip, the potentials -10.6 V, 2.65 V, -2.65 V and 10.6 V are applied on the on-chip electrodes and generate the quadrupole field shown in Fig. 3.7. This electric field exerts a force onto the Rydberg atoms, accelerating them towards the center of the guide. After 6.8 μs the guide is switched off and the electric field in the experimental setup is again solely given by the applied voltages on the stack electrodes.
The spatial distribution at this point is shown in Fig. 5.3 (a) and (b). In the x-y plane one observes that at the edges of the cloud, the atoms are slightly shifted upwards. This is due to the strong fields between the two outer on-chip electrodes, see Fig. 3.5 and 3.6 (a).
Compared to the initial shape of the atom cloud, the spatial distribution in the z-x plane is elongated along the beam axis, due to the spread of the relative kinetic energy of the atoms. However, the transverse confinement, as expected from the quadrupole guide, is not significant in the spatial distribution.
The transverse acceleration of the Rydberg atoms in the electric field is best analyzed in the phase space in the x - direction. Compared to the initial phase space, the distribution is rotated clockwise, shown in Fig. 5.3 (c). This rotation corresponds to an acceleration of the atoms towards the center of the guide, such that after the guide, the atoms with a negative

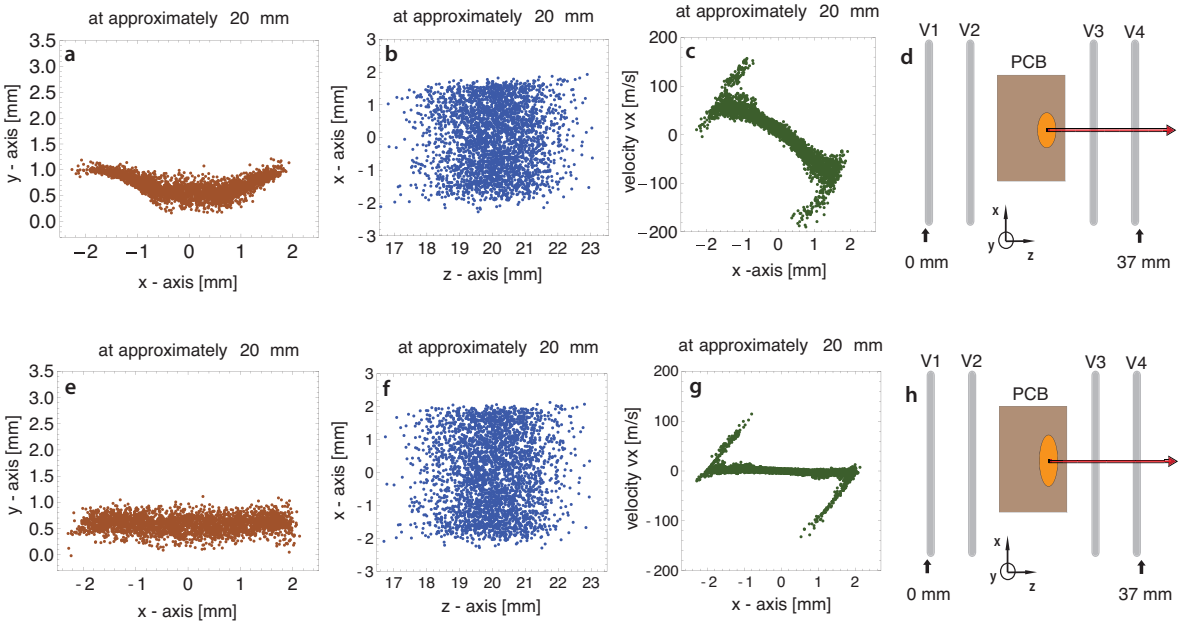

Figure 5.3.: (a) and (b) Spatial distribution of the Rydberg atoms after passing the quadrupole field. (c) Phase space distribution in the x - direction. Due to the acceleration in the quadrupole field, the distribution is rotated clockwise with respect to the initial distribution in Fig. 5.2 (c). (d) Position of the atom cloud above the PCB at the end of the guide. (e) – (h) Same plots as in the top row, but now if no potentials are applied on the on-chip electrodes.

x - coordinate have a positive velocity v_x.

If no potentials are applied on the on-chip electrodes, then the trajectories of the atoms are determined by the electric field generated by the stack electrodes. The same plots as discussed above are given for this case, with no applied quadrupole field, in Fig. 5.3 (e) to (h).

The sharp bending at the edges of the phase space distribution, see Fig. 5.3 (g), are due to the strong field strength very close to the openings of the electrode. Only the atoms far off the center are subject to these fields and are strongly deflected form the beam axis. This effect is discussed in more detail in Section 5.3.

Rydberg atoms in the ionization region

After the interaction with the quadrupole guide above the PCB, the atoms propagate into the ionization region. When the atoms are between electrode V3 and V4, a large voltage pulse is applied on electrode V3 in order to field ionize the Rydberg atoms and to accelerate the ionic core towards the MCP. Due to the low mass of the hydrogen atom and the strong fields, the proton will reach a very high longitudinal velocity[2]. Due to this, the spatial distribution in the ionization region will be mapped onto the MCP.

The spatial distribution in the ionization region is compressed in the transverse direction, shown in Fig. 5.4 (a) and (b), proofing that the applied potentials lead to the anticipated

[2]For the applied voltages specified in Section 5.1, the protons will reach velocities in the range of 7×10^5m/s

focusing of the Rydberg atoms. In the x-y plane, the distribution is elongated along the y axis, which is a consequence of the vertical acceleration of the atoms above the on-chip electrode at the edge of the cloud, observed in Fig. 5.3 (a).
Due to the applied quadrupole fields, the Rydberg atoms in the ionization region are mostly distributed along the beam axis in the z-x plane, see Fig. 5.4 (b). Compared to the case without the quadrupole field above the PCB, shown in Fig. 5.4 (f), the spatial confinement is very well apparent.
The acceleration of the Rydberg atoms in the quadrupole field towards the center of the guide leads to a 'vertical' phase space distribution in the ionization region, illustrated in Fig. 5.4 (c). This shows that the spatial distribution is small compared to the velocity spread of the Rydberg atoms. For the subsequent mapping of the spatial distribution onto the MCP, this transverse velocity is not relevant, as the acceleration of the ionic cores in the ionization field leads to a longitudinal velocity that is larger by three orders of magnitude.

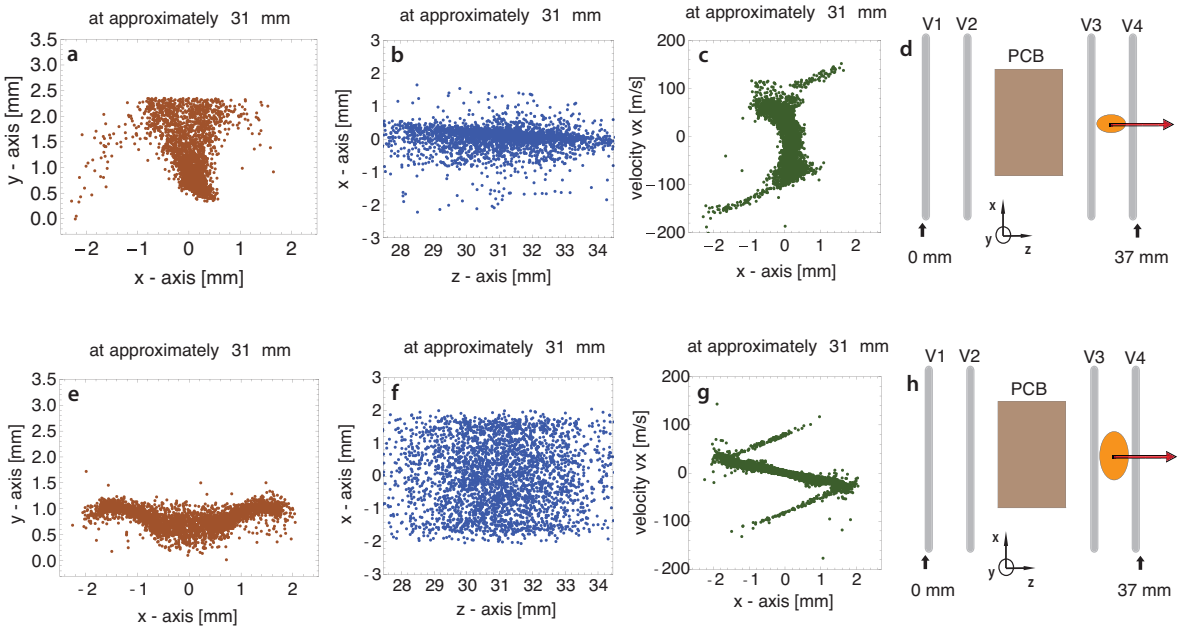

Figure 5.4.: (a) and (b) Spatial distribution of the Rydberg atoms in the ionization region. (c) Phase space density in the x - direction. The acceleration in the guide results in a 'vertical' distribution. (d) Position of the atom cloud with respect to the stack electrodes. (e)–(h) Corresponding plots if no quadrupole field is applied. The bending of the spatial distribution in (a) is due to the fields between the grounded on-chip electrodes and the stack electrodes.

Detection of the spatial distribution with the MCP detector

After the hydrogen Rydberg atoms are ionized and accelerated along the positive z - axis, their spatial distribution is recorded at the MCP detector, see Section 3.3. This is one of the main results obtained in the experiment.
The transverse distribution of the atoms at the MCP depends on the spatial distribution in

the ionization region, shown in Fig. 5.4 (a) and (b), and the applied electric fields. The velocity distribution of the Rydberg atoms is not relevant, as discussed in the previous section. Due to the holes in the electrodes along the beam axis, the electric field in the ionization region is not perfectly homogeneous, leading to ion optic effects. The atoms experience an acceleration pointing in the same transverse direction as their radial offset from the z - axis. In the current simulation this leads to a shift of the spatial distribution in positive y-direction. The transverse distribution at the MCP detector is shown for the case with the applied quadrupole field in Fig. 5.5 (a) and without guiding in Fig. 5.5 (b), respectively, demonstrating a clear difference. In the first case, the atoms are strongly confined in the x - direction, which is a direct consequence of the focusing in the ionization region. If the atoms are not guided, the atoms are spread along the full width of the MCP detector.
The clear results of this simulation suggests, that the effect of guiding and focusing of Rydberg atoms can be reproduced in the experiment; but it is to note, that in the simulation any atom - atom or atom - surface interaction was neglected. The interaction between the Rydberg atoms is expected to be small due to the low density and the low transverse velocity [33]. The interaction of the Rydberg atoms with the surface of the PCB at a short distance is not negligible because of the large dipole moment [40]. However, the atom surface distance in this experiment is much larger and is of the order of several hundred micro meter.

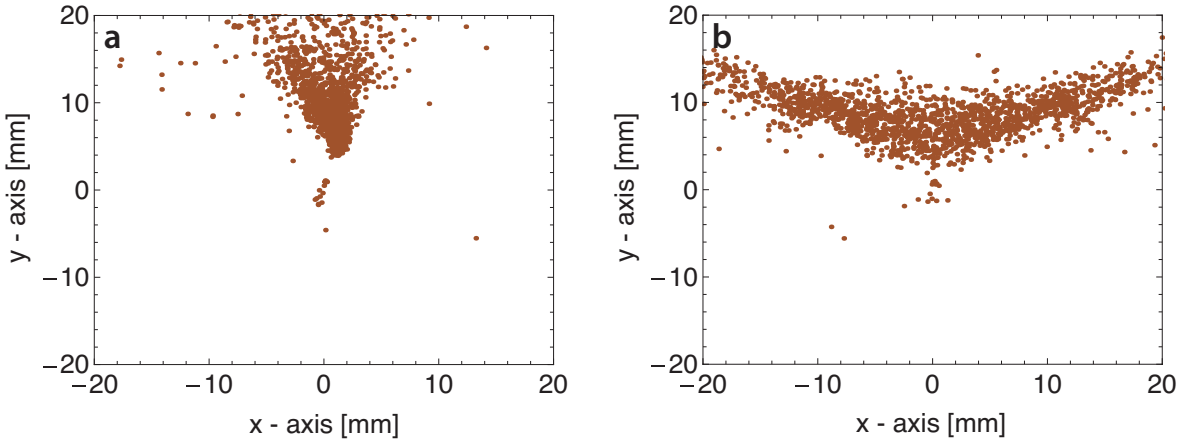

Figure 5.5.: Transverse spatial distribution of the Rydberg atoms at the position of the MCP detector. (a) If the quadrupole field above the PCB was 'ON', the Rydberg atoms are spatially confined in the x direction. (b) If the guide is turned 'OFF', this confinement is not observed.

5.3. Propagation of the atoms – additional information

Transverse acceleration upon passing the stack electrode

The initial distribution in the phase space in x - direction is shown in Fig. 5.2 (c). If no force was exerted onto the atoms, this distribution would be stretched along the x - axis while evolving in time. However, even if no quadrupole field is applied, one observes that the phase

space is slightly rotated, such that the distribution is essentially a horizontal line between the stack electrode V2 and V3, see Fig. 5.3 (g). This corresponds to an acceleration towards the beam - axis.
The reason for this acceleration is that the Rydberg atoms see a field gradient while they pass the opening in the stack electrode V2. The field distribution in this region is shown in Fig. 5.6.
The equipotential lines of the electric field in the transverse plane indicate that the gradient points radially outwards from the center. This leads to a force towards the beam axis for the low-field seeking states, explaining the acceleration of the Rydberg atoms and the rotation of the phase space distribution, see Fig. 5.3 (g).

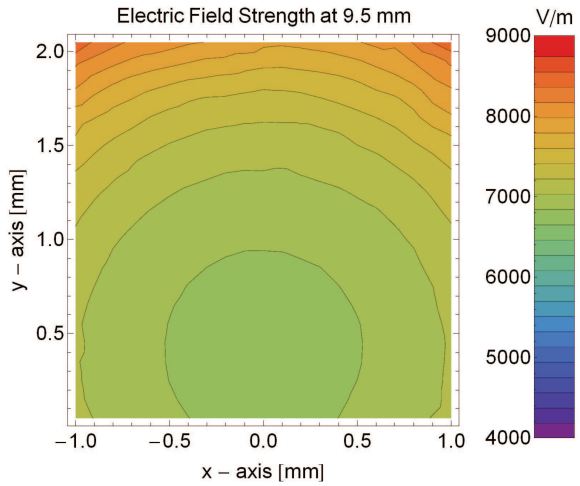

Figure 5.6.: Equipotential lines of the electric field strength in the opening of the stack electrode 2, see Fig. 3.1. The field strength increases with the radial distance from the center. The y - axis is the vertical distance from the chip surface.

Deflection at the stack electrode

The sharp bending of the phase space at the edge, see Fig. 5.3 (g) or Fig. 5.4 (g), is another secondary effect when the atoms pass the opening in the electrode. The edges of the metal structure at the opening of the electrode lead to strong field gradients and an acceleration of the Rydberg atoms. Only atoms far off the center, therefore only atoms at the edge of the cloud, see these fields and are deflected from the propagation direction.
This effect is negligible in the y - direction: Due to the smaller extend of the cloud in this dimension, the Rydberg atoms do not come close enough to the electrode in order to observe the effect.

5.4. Guiding the atoms with a stronger quadrupole field

If higher potentials are applied on the on-chip electrodes, the force exerted onto the atoms is stronger and the atoms are focused at a different point. A further increase would even lead to a transverse oscillation within the quadrupole guide.
In this section the trajectories of the Rydberg atoms are analyzed if −40 V, 10 V, −10 V and 40 V are applied on the guide electrodes, see Fig. 3.5. This corresponds to the case discussed in Section 3.4.2.
After the guide, the atom cloud is slightly compressed in transverse direction, see Fig. 5.7 (a) and (b), but not yet focused. Due to the acceleration in the quadrupole field, the transverse velocity is high, shown in Fig. 5.7 (c). As after the guide the restoring force acting on the Rydberg atoms towards the center no longer applies, the atom cloud can freely expand in the transverse direction.
The MCP signal depends on the spatial distribution in the ionization region and is observed

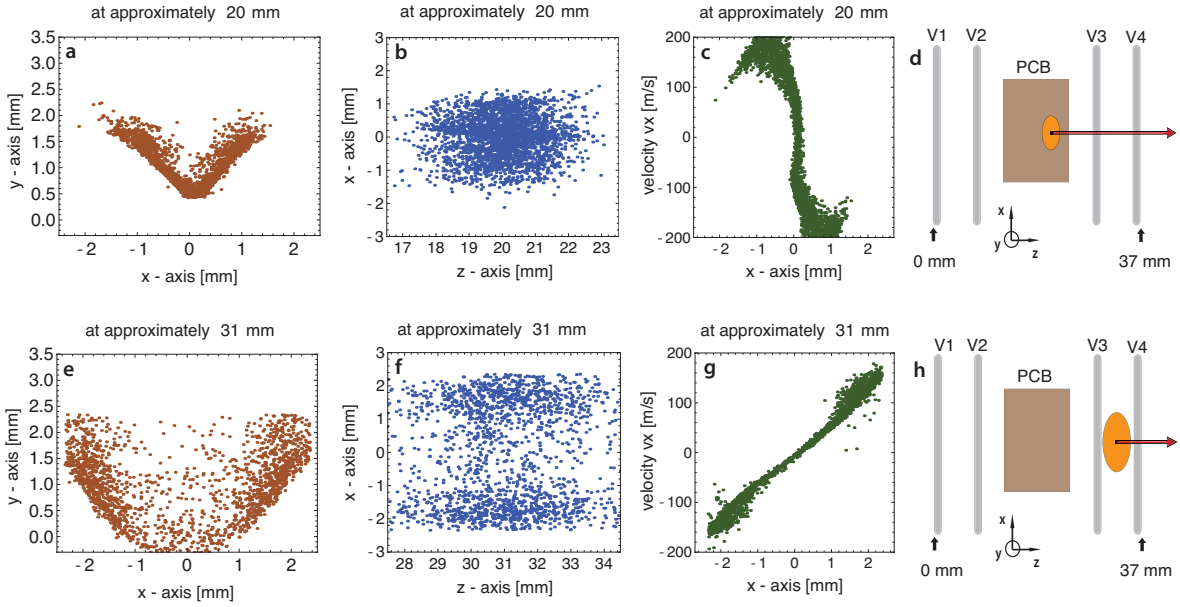

Figure 5.7.: (a) and (b) Spatial distribution of the Rydberg atoms after the quadrupole guide, if −40 V, 10 V, −10 V and 40 V are applied on the on-chip electrodes. Due to the larger applied potentials, the vertical acceleration at the edge of the cloud is more pronounced than in the previous simulation, see Fig. 5.3. (c) Phase space distribution in the x - direction. (d) Position of the atom cloud with respect to the stack electrodes. (e) – (h) Atom cloud in the ionization region. The atoms are spread within a large volume, such that this spatial distribution cannot efficiently be mapped onto the MCP.

in the experiment. In the case of focusing (Section 5.2), the transverse position spread was minimal there, and the spatial distribution of the Rydberg atoms showed a clear structure at the MCP detector, see Fig. 5.5.
In the present case, however, the atom cloud is focused 11 mm before the ionization, corresponding to a propagation time of around 15 μs. Due to the velocity distribution after the guide, the atom cloud is considerably extended in the transverse direction during this time.

The majority of the atoms in the ionization region are therefore far off the z - axis, shown in Fig. 5.7 (e) to (g). In addition, due to ion optic effects only a small fraction of the atoms finally reaches the MCP detector, and the spatial distribution is basically homogeneous there.

These simulations predict that with the proposed voltage configuration the atoms can be confined in transverse direction above the chip, but it is not possible to directly image this effect onto the MCP detector. The reason for this is the transverse velocity of the atoms combined with the relatively long distance from the end of the guide to the ionization region, such that the atom cloud will expanded to a large volume.
To see an effect of the quadrupole guide on the MCP detector – different from the focusing – would be to further increase the trap potential, such that the atom cloud is focused in the first half of the guide and transversally decelerated in the second half. The potentials to achieve this are −260 V, 65 V, −65 V and 260 V on the on-chip electrodes[3].
However, with this potential configuration it is not possible to decelerate a majority of the atoms to a low transverse velocity at the end of the guide, as it is illustrated in the phase space in Fig. 5.8 (a). The reason is the anharmonicity of the quadrupole potential, which leads to the spiraling of the phase space distribution, such that only a small fraction of the atoms is finally slowed down in the transverse direction. A similar effect was observed in the trapping experiment in Section 4.5.1. Consequently, the spatial distribution in the ionization region is basically homogeneous here as well, as shown in Fig. 5.8 (b).

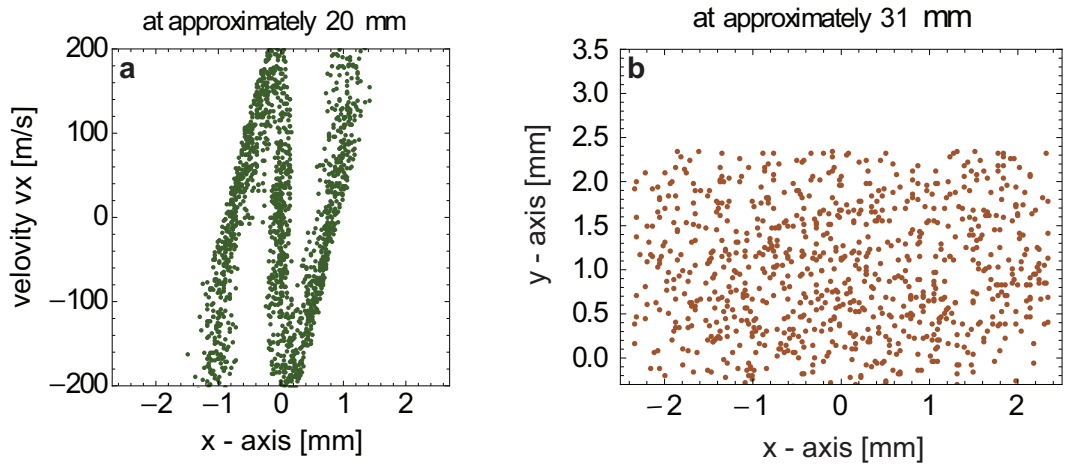

Figure 5.8.: (a) Phase space density distribution in x - direction after the guide, for −260 V, 65 V, −65 V and 260 V on the on-chip electrodes. (b) Transverse spatial distribution in the ionization region.

[3]These values actually seem to be too high to be applied on the on-chip electrodes. However, for the simulations there is of course no technical limit.

6. Conclusion and Outlook

In this thesis a simulation program to calculate the trajectories of Rydberg atoms in the experimental setup has been developed. This allows to study the effects of electric fields on the atoms and to predict the signal on the MCP detector, which is important for the interpretation and analysis of the experimental results.
Another application is the testing of different designs of the setup and in particular the arrangement of on-chip electrodes, as both are not definite yet. The trajectory simulations allow to carefully investigate the properties of each element and to try different approaches in order to optimize the experimental setup accordingly.
In the realm of this thesis, a first version of an on-chip quadrupole guide for the Rydberg atoms has been designed and investigated with the simulation program. It was shown that the proposed guide can be used to focus the atoms at a specific point and to subsequently observe this effect at the MCP detector. The experimental realization of this system will allow to draw conclusions for future setups, with the aim to guide Rydberg atoms at a short distance above a microwave transmission line.
First experiments with the Rydberg atoms will be performed in the near future. The effects of the chip surface and the electric fields generated by on-chip electrodes on the Rydberg atoms will be studied and can be analyzed by comparing the results with the simulations. In a later stage the interaction with microwave fields of a transition line resonator will be investigated. This includes the driving of transitions between different Stark states of the atoms with the microwave radiation, as well as observing shifts in the resonance frequency of the resonator, depending on the state of the Rydberg atom.

Bibliography

[1] D. P. DiVincenzo. The physical implementation of quantum computation. *Fortschritte der Physik*, 48(9-11):771–783, 2000.

[2] A. Einstein, B. Podolsky, and N. Rosen. Can quantum-mechanical description of physical reality be considered complete? *Phys. Rev.*, 47(10):777–780, May 1935.

[3] Alain Aspect, Philippe Grangier, and Gerard Roger. Experimental realization of einstein-podolsky-rosen-bohm gedankenexperiment: A new violation of bell's inequalities. *Phys. Rev. Lett.*, 49:91–94, 1982.

[4] Rowe, Kielpinski, Meyer, Sackett, Itano, Monroe, and Wineland. Experimental violation of a bell's inequality with efficient detection. *Nature*, 409, 2001.

[5] Markus Ansmann, H. Wang, Radoslaw C. Bialczak, Max Hofheinz, Erik Lucero, M. Neeley, A. D. O'Connell, D. Sank, M. Weides, J. Wenner, A. N. Cleland, and John M. Martinis. Violation of bell's inequality in josephson phase qubits. *Nature*, 461(7263):504–506, September 2009.

[6] R. P. Feynman. Simulating physics with computers. *International Journal of Theoretical Physics*, 21(6):467–488, June 1982.

[7] Peter W. Shor. Polynomial-time algorithms for prime factorization and discrete logarithms on a quantum computer. *SIAM Journal on Scientific and Statistical Computing*, 26:1484, 1997.

[8] Michael A. Nielsen and Isaac L. Chuang. *Quantum Computation and Quantum Information*. Cambridge Univertity Press, 2000.

[9] Rainer Blatt and David Wineland. Entangled states of trapped atomic ions. *Nature*, 453(7198):1008–1015, June 2008.

[10] Ronald Hanson and David D. Awschalom. Coherent manipulation of single spins in semiconductors. *Nature*, 453(7198):1043–1049, June 2008.

[11] John Clarke and Frank K. Wilhelm. Superconducting quantum bits. *Nature*, 453(7198):1031–1042, June 2008.

[12] Serge Haroche and Jean-Michel Raimond. *Exploring the Quantum: Atoms, Cavities, and Photons*. OUP Oxford, 2006.

[13] R.J. Schoelkopf and S.M. Girvin. Wiring up quantum systems. *Nature*, 451:664, 2008.

[14] Tatjana Wilk, Simon C. Webster, Axel Kuhn, and Gerhard Rempe. Single-atom single-photon quantum interface. *Science*, 317(5837):488–490, 2007.

[15] A. Blais, R.-S. Huang, A. Wallraff, S. M. Girvin, and R. J. Schoelkopf. Cavity quantum electrodynamics for superconducting electrical circuits: An architecture for quantum computation. *Phys. Rev. A*, 69(6):062320, June 2004.

[16] A. Wallraff, D. I. Schuster, A. Blais, L. Frunzio, R. S. Huang, J. Majer, S. Kumar, S. M. Girvin, and R. J. Schoelkopf. Strong coupling of a single photon to a superconducting qubit using circuit quantum electrodynamics. *Nature*, 431:162–167, 2004.

[17] G. Ithier, E. Collin, P. Joyez, P. J. Meeson, D. Vion, D. Esteve, F. Chiarello, A. Shnirman, Y. Makhlin, J. Schriefl, and G. Schön. Decoherence in a superconducting quantum bit circuit. *Phys. Rev. B*, 72(13):134519, Oct 2005.

[18] L. DiCarlo, J. M. Chow, J. M. Gambetta, Lev S. Bishop, B. R. Johnson, D. I. Schuster, J. Majer, A. Blais, L. Frunzio, S. M. Girvin, and R. J. Schoelkopf. Demonstration of two-qubit algorithms with a superconducting quantum processor. *Nature*, 460(7252):240–244, July 2009.

[19] P. Rabl, D. DeMille, J. M. Doyle, M. D. Lukin, R. J. Schoelkopf, and P. Zoller. Hybrid quantum processors: Molecular ensembles as quantum memory for solid state circuits. *Phys. Rev. Lett.*, 97(3):033003, July 2006.

[20] Anders S. Sørensen, Caspar H. van der Wal, Lilian I. Childress, and Mikhail D. Lukin. Capacitive coupling of atomic systems to mesoscopic conductors. *Phys. Rev. Lett.*, 92(6):063601, Feb 2004.

[21] S. D. Hogan and Merkt F. Demonstration of three-dimensional electrostatic trapping of state-selected rydberg atoms. *Phys. Rev. Lett.*, 100:043001, 2008.

[22] R.F. Stebbings and F.B. Dunning. *Rydberg states of atoms and molecules*. Cambridge Univerity Press, 1983.

[23] Thomas F. Gallagher. *Rydberg Atoms*. Cambridge University Press, 1994.

[24] Hermann Haken and Hans Christoph Wolf. *Atom- und Quantenphysik*. Springer, 1996.

[25] Hans A. Bethe and Edwin E. Salpeter. *Quantum mechanics of one- and two- electron atoms*. Plenum/Rosetta, 1977.

[26] F. Merkt. Molecules in high rydberg states. *Annu. Rev. Phys. Chem.*, 48:675–709, 1997.

[27] Franz Schwabel. *Quantenmechanik*. Springer, 2007.

[28] L.D. Landau and E.M. Liefschitz. *Quantenmechanik*. Akademie-Verlag Berlin, 1979.

[29] Edward Vliegen. *Rydberg states in atom and molecule optics*. PhD thesis, ETH Zurich, 2006.

[30] E. Vliegen and F. Merkt. On the electrostatic deceleration of argon atoms in high rydberg states by time-dependent inhomogeneous electric fields. *Journal of Physics B*, 38:1623–1636, 2005.

[31] S. D. Hogan, A. W. Wiederkehr, M. Andrist, H. Schmutz, and F. Merkt. Slow beams of atomic hydrogen by multistage zeeman deceleration. *Journal of Physics B*, 41:081005, 2008.

[32] R. J. Damburg and V. V. Kolosov. A hydrogen atom in a uniform electric field iii. *Journal of Physics B*, 12:2637–2643, 1979.

[33] Stephen Hogan, 2010. Private communications.

[34] E. Vliegen, S. D. Hogan, H. Schmutz, and F. Merkt. Stark deceleration and trapping of hydrogen rydberg atoms. *Phys. Rev. A*, 76(2):023405, 2007.

[35] E. Vliegen, P. A. Limacher, and F. Merkt. Measurement of the three-dimensional velocity distribution of stark-decelerated rydberg atoms. *Eur.Phys.J.D*, 40:73–80, 2006.

[36] M. H. Devoret, A. Wallraff, and J. M. Martinis. Superconducting qubits: A short review. *cond-mat/0411174*, -, 2004.

[37] Thomas Alfred Paul. *Development and spectroscopic applications of a solid-state vacuum ultraviolet laser system in atomic and molecular physics*. PhD thesis, ETH Zurich, 2008.

[38] J. Mozley, P. Hyafil, G. Nogues, M. Brune, J.-M. Raimond, and S. Haroche. Trapping and coherent manipulation of a rydberg atom on a microfabricated device: a proposal. *The European Physical Journal D*, 35:43–57, 2005.

[39] Joseph Ladislas Wiza. Microchannel palate detectors. *Nuclear Instruments and Methods*, 162:587–601, 1979.

[40] A. Tauschinsky, R. M. T. Thijssen, S. Whitlock, H. B. van Linden van den Heuvell, and R. J. C. Spreeuw. Spatially resolved excitation of rydberg atoms and surface effects on an atom chip. arXiv:1004.3230v1, 2010.

[41] J. M. McGuirk, D. M. Harber, J. M. Obrecht, and E. A. Cornell. Alkali-metal absorbate polarization on conducting and insulating surface probed with bose-einstein condensates. *Phys. Rev. A*, 69:062905, 2004.

[42] J. M. Obrecht, R. J. Wild, and E. A. Cornell. Measuring electric fields from surface contaminants with neutral atoms. *Phys. Rev. A*, 75:062903, 2007.

[43] John David Jackson. *Klassische Elektrodznamik*. deGruyter, 2006.

[44] Hans J. Herrmann. Introduction to computational physics. Lecture notes.

[45] *Ansoft Maxwell manual*.

[46] E. Vliegen and F. Merkt. Normal-incidence electrostatic rydberg atom mirror. *Phys. Rev. Lett.*, 97(3):033002, 2006.

[47] Alfio Quarteroni, Riccardo Sacco, and Fausto Saleri. *Numerische Mathematik 2*. Springer, 2002.

[48] Stephen Prata. *C primer plus*. Sams, 2002.

[49] Mark Galassi. *Gnu Scientific Library Reference Manual*. Network Theory Limited, 2006.

A. Units and constants

A.1. Atomic units

Quantity	Symbol	Value	Unit
Unit of charge	e	$1.60217653(14) \times 10^{-19}$	C
Unit of mass	m_e	$9.1093826(16) \times 10^{-31}$	kg
Unit of action	$\hbar$	$1.05457168(18) \times 10^{-34}$	Js
Unit of length	a_0	$0.5291772108(18) \times 10^{-10}$	m
Unit of energy	$E_h = \frac{\hbar^2}{a_0^2 m_e}$	$4.35974417(75) \times 10^{-18}$	J
Unit of time	$\frac{\hbar}{E_h}$	$2.418884326505(16) \times 10^{-17}$	s
Unit of force	$\frac{E_h}{a_0}$	$8.2387225(14) \times 10^{-8}$	N
Unit of velocity	$\frac{a_0 E_h}{\hbar}$	$2.1876972633(73) \times 10^{6}$	$\frac{m}{s}$
Unit of electric potential	$\frac{E_h}{e}$	27.2113845(23)	V
Unit of electric field strength	$\frac{E_h}{a_0 e}$	$5.14220642(44) \times 10^{11}$	$\frac{V}{m}$

Table A.1.: Atomic units [29, 25]

In this unit system it is:

$$\hbar = 1$$
$$e = 1$$
$$c = 137.036 = \frac{1}{\alpha}$$
$$\varepsilon_0 = \frac{1}{4\pi}$$
$$R_\infty = \frac{1}{2}$$

Table A.2.: Some important constants in atomic units

Acknowledgment

I would like to say THANK YOU to

Professor Andreas Wallraff, for giving me the opportunity to work on this exciting new experiment in the QUDEV lab. The topic of the thesis and the project itself lead to a very rewarding time for me in this research group.

Professor Frédéric Merkt, for his interest in my work. His critical questions, his ideas and suggestions during the 'Rydberg - meetings' were very important for the progress of my thesis.

Stefan Filipp, for his kind support during my master thesis. Apart from his physical understanding, I of course particularly appreciated his *Mathematica* - skills. Specially I am thankful for the proofreading of my thesis and the many suggestions to improve it.

Stephen Hogan, for sharing his knowledge with me. Stephen was an inexhaustible source for answers to all sorts of questions ranging from A like atomic units to Z like Zeeman deceleration. In particular I would like to thank him for the time he sacrificed for the 'r^2 issue'.

Silvio Marx, for sharing his cookies with me. It was enjoyable to work together on the Rydberg experiment, to share the office with him, and in particular to play table tennis with our own stupid rules.

Hansjürg Schmutz, for being a patient teacher in electronics. Only with his experience it was possible to develop a simulation of the electronic properties of the experimental setup.

The whole QUDEV team for the nice and welcoming atmosphere. It was a great pleasure to stay here.